Effect of tool profile and fatigue loading on the local hardness around scratches in clad and unclad aluminium alloy 2024

Journal Item

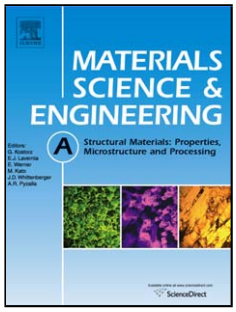

Title: Effect of Tool Profile and Fatigue Loading on the Local Hardness Around Scratches in Clad and Unclad Aluminium Alloy 2024

Authors: M.K. Khan, M.E. Fitzpatrick, S.V. Hainsworth, L. Edwards

PII: S0921-5093(09)00813-2
DOI: doi:10.1016/j.msea.2009.07.035
Reference: MSA 25404

To appear in: *Materials Science and Engineering A*

Received date: 23-5-2009
Accepted date: 17-7-2009

Please cite this article as: M.K. Khan, M.E. Fitzpatrick, S.V. Hainsworth, L. Edwards, Effect of Tool Profile and Fatigue Loading on the Local Hardness Around Scratches in Clad and Unclad Aluminium Alloy 2024, *Materials Science & Engineering A* (2008), doi:10.1016/j.msea.2009.07.035

This paper reports measurements of the hardness changes produced in clad and unclad 2024 aluminium from a scratching process. Two different tools were used that produced different scratch profiles and levels of plastic damage.

We have shown that the local hardness can be mapped using nanoindentation, and correlated the changes in hardness with quantitative information on the plastic damage from synchrotron X-ray diffraction. The changes can be related to the different cutting mechanisms observed for the two tools.

Specimens subjected to fatigue loading did not show any change in the hardness profile around the scratch.

We believe that the measurements and interpretation, combining nanoindentation and synchrotron X-ray techniques, are entirely novel.

Effect of Tool Profile and Fatigue Loading on the Local Hardness Around Scratches in Clad and Unclad Aluminium Alloy 2024

M. K. Khan[1], M. E. Fitzpatrick[1], S. V. Hainsworth[2], L. Edwards[1,3]

[1] Materials Engineering, The Open University, Walton Hall, Milton Keynes MK7 6AA, UK

[2] Department of Engineering, University of Leicester, Leicester LE1 7RH, UK

[3] Currently at: Australian Nuclear Science and Technology Organisation, PMB1, Menai, NSW 2234, Australia

Abstract

Nanoindentation has been used to study the hardness changes produced by scratching of aluminium alloy AA2024, with and without a clad layer of pure aluminium. The hardness was mapped around scratches made with diamond tools of different profiles. One tool produced significant plastic damage with associated hardening at the scratch root, whilst the other produced a 'cleaner' cut with no hardening. The different behaviours and are attributed to whether the tool makes the scratch by a 'cutting' or a 'ploughing' mechanism. The degree of plastic damage around the scratches has been correlated with peak broadening data obtained using synchrotron X-ray diffraction.

There was no change observed in the local hardness around the scratch with fatigue loading.

1. Introduction

High-strength, low-weight aluminium alloy components are widely used in aerospace structural applications. Aluminium alloy 2024-T351 is used in structural areas of the fuselage and wings where high stiffness, good strength and good fatigue performance is required. Additional corrosion resistance is obtained by roll-bonding commercially-pure Al-cladding to the material.

Whilst the aircraft is in service, damage such as scratches and pits can occur to the surface of the aluminium-clad system. The scratch morphology will vary depending on the mechanism of scratch formation, the forces involved, and the geometry of the object which caused the scratch. Fatigue cracks can grow and propagate from the base of these scratches, and the resultant fatigue life is highly influenced by the manner in which the scratch was produced. If a scratch is caused accidentally during a maintenance operation, for example, different tools will generate differing levels of residual stress around the scratch root, and the magnitude and extent of the residual stress field influence the way in which cracks from the root propagate in fatigue. The scratch geometry and sharpness of the root radius also affect crack initiation and propagation.

The residual stress that is generated during scratching is small and localized around the scratch root [1, 2]. In order to measure such residual stresses, a technique which has a spatial scale of a few microns is required. Nanoindentation techniques allow determination of the

mechanical properties of materials in very small volumes. Several techniques have been developed to extract residual stresses from nanoindentation load-displacement curves [3-7]. However, in addition to residual stress, the load-displacement curve is also sensitive to effects such as work-hardening of the material around the scratch root. Thus around any scratch, the nanoindentation load-displacement curve response is a convolution of materials properties, work hardening and residual stress.

Hence in this study we are investigating the changes in hardness in the material when a scratch is produced. The results give information on the mechanism by which the scratches are produced, which will be used in the broader study for development of a method for extracting residual stress data from the nanoindentation load-displacement curves.

2 Theoretical Background

Depth-sensing indentation allows the determination of mechanical properties at very low loads and displacements. An indenter of known geometry is driven into the material surface by applying a known load, and the load-displacement data is analysed. As the indenter is driven into the material, both elastic and plastic deformation processes occur, producing a hardness impression that corresponds to the shape of the indenter. The total penetration depth is the summation of the elastic and plastic deformations of the material beneath the indenter tip. The plastic depth is used to determine the contact area. During unloading, only the elastic portion of the displacement is recovered, and this effectively allows separation of the elastic properties of the material from the plastic. A schematic representation of indentation load P versus displacement h obtained during one full cycle of loading and unloading is presented in Figure 1.

One of the more commonly used methods for analyzing nanoindentation load-displacement data is that of Oliver and Pharr [8]. In the Oliver-Pharr method, hardness and elastic modulus are determined from indentation data obtained during one complete cycle of loading and unloading. According to this method, the unloading curve is fitted to the power-law relation:

$$P = B\left(h - h_f\right)^m \qquad (1)$$

where P is the indentation load, h is the displacement, B and m are empirically-determined fitting parameters, and h_f is the final displacement after complete unloading. The depth along which contact is made between the indenter and the specimen, h_c, can also be estimated from the load-displacement data using:

$$h_c = h_{\max} - \varepsilon\frac{P_{\max}}{S} \qquad (2)$$

where $h_{\max}$ is the maximum depth of penetration at $P_{\max}$, the peak indentation load, and ε is a constant which depends on the geometry of the indenter: for a Berkovich indenter ε=0.75.

Once the parameters B and m are obtained by curve fitting, the initial unloading stiffness S can be established by differentiating Eq. (1) at the maximum depth of penetration, $h = h_{\max}$:

$$S = \left(\frac{\mathrm{d}P}{\mathrm{d}h}\right)_{h=h_{\max}} = mB\left(h_{\max} - h_f\right)^{m-1} \qquad (3)$$

The hardness is then determined by the relationship

$$H = \frac{P}{A} \qquad (4)$$

where H is hardness, P is the load and A is the projected contact area at that load. The projected contact area of the hardness impression, A, is derived by evaluating an empirically determined indenter shape function at the contact depth, h_c; that is, $A = f(h_c)$. To a first approximation, the shape function, $A = 24.5\ h_c^2$ relates the cross-sectional area of the indenter to the contact depth, although calibration of the indenter function is required to allow for deviations from a perfect indenter tip shape at small indenter penetrations.

The elastic modulus is determined from a modified form of Sneddon's relationship [9], *viz*:

$$E_r = \frac{\sqrt{\pi}}{2\beta}\frac{S}{\sqrt{A}} \qquad (5)$$

where E_r is the reduced elastic modulus, S is stiffness and β is a constant that depends on the geometry of the indenter. For indenters of triangular cross-section like the Berkovich and cube-corner indenters, $\beta = 1.034$. The reduced modulus, E_r is used to account for the fact that elastic displacements occur in both the indenter and the sample. The elastic modulus of the test material, E_s, is calculated from E_r using:

$$\frac{1}{E_r} = \frac{1-\nu_i^2}{E_i} + \frac{1-\nu_s^2}{E_s} \qquad (6)$$

where E_s and ν_s are the elastic modulus and Poisson's ratio for the test material; and E_i and ν_i are the elastic modulus and Poisson's ratio for the indenter. For diamond, the elastic constants $E_i = 1140$ GPa and $\nu_i = 0.07$ are usually used.

3. Materials and Experimental details

3.1 Material details

The materials used in this study were in the form of cold rolled plate of Al2024-T351 of 2 mm total thickness, with an aluminium cladding of 80 μm on both faces as shown in Fig. 2. Some samples of Al2024 were also prepared without cladding by chemical milling of the clad material, leaving only 2024. The grain size of the Al2024-T351 was determined by quantitative metallography and electron back scattered diffraction (EBSD), and was found to be ~20 μm. Figure 3a shows a secondary electron image and figure 3b shows an EBSD image of the surface of the Al2024-T351 plate. It can be seen from the EBSD image that the grains are randomly oriented in the Al-plate. The grain size of the Al-clad was not measured directly here owing to the difficulties of preparing metallographic samples of such a thin, soft layer which is difficult to etch, but previous work has shown it to be in the range 30 – 70 μm.

3.2 Introduction of Scratches

Various scratches were made using two different automated diamond tools. A schematic of a typical scratch geometry is shown in figure 4. The scratch has a notch depth b, width a, root radius R, and a notch angle of 2θ. Two tools were used, designated tool A and tool B. An example of the different scratch profiles generated by these tools is shown in figure 5.

Scratches made by both tools resulted in a scratch root radius of ~5 μm. Tool A generated scratches with a non-symmetric cross-section (figure 5a), which was seen on all scratches made with this tool and which was caused by a flaw on the tool.

Scratches were made to controlled depths, but elastic recovery of the scratches after the load was removed, and the different forces required for the two tools, meant that in practice for an initial set depth the residual scratches from tool A were 10% deeper than scratches made with tool B.

Scratches were produced in clad and unclad Al 2024-T351. Owing to differences in the work hardening exponents and *E/H* ratios (table 1) for the pure aluminum cladding and the Al 2024-T351, different extents of plastic deformation were obtained around the resultant scratch tracks. This plastic deformation plays an important role in fatigue crack initiation and propagation from the roots of these scratches.

After the scratches were made, the coupons were cross-sectioned and polished and etched to reveal the extent of the plastic deformation, and for nanoindentation testing.

Scratches were made with both tools to two different depths in the clad samples: scratches with a depth of 50 μm (less than the clad thickness) and scratches with a depth of 100 μm (greater than the clad thickness). Scratches were also made into unclad Al2024-T351 to depths of 50, 75, and 100 μm.

3.3 Nanoindentation testing

The mechanical properties of the Al-Clad and substrate Al2024-T351 were characterized using an MTS Nanoindenter XP system with a Berkovich indenter tip. The instrument was operated in basic hardness load-displacement mode, which simply records load, displacement and time. Indentations were made using a constant nominal strain rate ($\dot{P}/P$) of 0.05 s^{-1} and drift rate of 0.05 nm s^{-1}. Indentations were made to depths of 600 nm. Our previous studies [10] have shown that indentations in these materials have a minimum of pile-up at this indentation depth. Indentations were made in an array around the scratch cross-section with 20 μm spacing between the indentations. The first row of indentations was made at a distance of 10 μm from the surface of the cladding and subsequent rows were spaced 20 μm apart. Figure 6 shows the arrangement of indentations in greater detail.

3.4 Fatigue testing

Four-point bend samples were prepared of size 50 mm × 210 mm × 2mm for the clad Al 2024-T351 and 50 mm × 210 mm × 1.8 mm for the unclad Al2024-T351. Samples were tested at a maximum stress of 200 MPa and a frequency of 5 Hz.

11 different samples were fatigue tested. Nine samples were tested to failure and two further samples, with scratches made by tool A, were fatigued to 250 000 and 500 000 cycles in the unclad Al2024-T351 samples. These cycles were well below the fatigue life of those particular samples, to observe the effect of cyclic loading on the hardness at the scratch root. After cycling, hardness mapping tests were conducted around the scratch routes in the same way as for the un-fatigued samples.

3.5 Synchrotron X-ray diffraction

A map of the local strain variation around the scratches was made using the ID31 diffractometer at the European Synchrotron Radiation Facility (ESRF), Grenoble, France. Data was obtained by diffraction from the (311) planes of the aluminium. The width of the diffraction peaks contains information on the microstresses in the material, which in turn are influenced by plastic damage [11, 12]: the local stress fields around dislocations collectively act to broaden Bragg diffraction peaks.

Measurements were made on 5091 aluminium, produced by a powder metallurgy process, which is ideal for synchrotron measurement owing to its fine grain size (~0.5 μm). This allows good diffraction data to be obtained even with a very small sampling gauge volume. The 2024 material has a larger grain size and some crystallographic texture, which did not allow for good data acquisition using synchrotron X-rays with a fine sampling volume. The 5091 was scratched using identical conditions to the 2024, to see the hardening behaviour around the scratch profile.

Diffraction peaks were obtained using an X-ray beam with dimensions ~80 × 50 μm^2. Coupons of dimension ~20 mm × 20 mm were extracted from scratched plates, and measurements were made of the strain component transverse to the scratch line. In this paper we report only the peak width data to provide correlation with the measured hardness changes. The scratch location was determined by careful wall scanning, where the scratch position was identified from the change in intensity as the gauge volume is translated through the sample surface and across the scratch.

A Gaussian profile was fitted to each diffraction peak.

4 Results and Discussion

4.1 Scratch profiles

The scratch cross-sections were examined by scanning electron microscopy, which revealed that for tool A, the scratch cross-section was not symmetric. There was an abrupt change in scratch profile on one side of scratch track as shown in Figure 5a. This irregularity was present in every scratch produced by this particular tool. For tool B the scratch cross-section was axisymmetric, and no irregularity in morphology was present, as shown in Figure 5b.

For both tools, pile-up of material was observed around the scratch track. For tool A the pile-up was more severe compared to tool B (figure 7). Due to the irregular shape of tool A, the pile-up was not symmetric, with more pile-up on the side of the scratch which showed irregularity in profile as shown in Fig. 7a.

For tool A, the extent of material displaced around the scratch track was greater. A ‘rough’ scratch track, with deformed material or debris around the scratch was seen. The scratching of the surface had clearly been associated with a large amount of plastic deformation and displacement of material, rather than a cutting action by which material is simply removed. This phenomenon, in which material is deposited around the edges of a scratch in the form of plastic pads is known as “ploughing”.

In contrast, a very smooth scratch track was obtained for tool B, with very little deformed material around the scratch (figure 7b). This tool was clearly removing material by a cutting action, rather than by plastic deformation and displacement of material by the tool.

The difference in terms of the depth and width, and the irregular profile of scratch cross-section demonstrates that these two tools are different from each other when scratching. It has been reported that the shape of the tool, and in particular the 'attack angle' between the leading edge of the tool and the workpiece, along with the shear strength at the interface between the cutting tool and the surface, have a significant effect on deformation behavior around scratches. For example, Mezlini *et al.* [13], Kato [14] and Subramanian [15] showed that abrasive wear mechanisms depend on the tool shape, attack angle, and test parameters. Tkaya *et al.* [16] observed the effect of tool attack angle on the wear mechanism. He found that for 30˚ attack angle the material was pushed primarily to the sides of the scratches, and a wedge was formed to the side and in front of the indenter without any loss of material. However for a 60˚ attack angle a transition of wear mechanism from ploughing to cutting, with chips in front of the indenter, was observed. Here the two tools produced different morphologies of scratches and different levels of deformation around the scratches. From figure 5 it can be seen that the tool profiles are significantly different, and although the images do not give information directly about the attack angle, the tool profiles suggest that Tool A has an attack angle of ~40˚ whilst for tool B the figure is closer to 30˚. Analysis of the cutting tracks indicates that that tool A is tending towards a ploughing action, while tool B is just cutting the material during scratching.

4.2 Hardness maps

4.2.1 Unclad material

The hardness environment around scratches with depths of 50 µm, 75 µm and 100 µm from both tools were investigated. In total five rows of indentations were made around each scratch as shown in Fig. 6. The hardness results were found to be independent of the scratch depth in this range, so here results of only the 75 µm deep scratch from tool A and the 100 µm deep scratch from tool B are presented.

For scratches from tool A, hardness values were constant in the first two rows of indentations from the surface, which indicated there was no localized hardening effect in this region. The first row of indents was actually slightly too close to the surface, giving hardness measurements that were lower by 5-8%.

For the next three rows of indentations a distinct localized hardening effect was seen close to the scratch. The effect of this localized deformation extended up to 150 µm from the scratch center as shown in Figure 8a. The effect of increased hardness was present on both sides of the scratch, although the hardening was not symmetric. The hardness was higher beneath the irregular feature on the tool, where the hardness increased as much as 35%. For the other side the hardness increase was around 25%. This indicates that there was greater deformation below the irregular feature observed on the tool.

For the 50 μm and 100 μm scratches from tool B, the hardness values remained constant for all the rows of indentations (figure 8b) indicating that there is no localized work hardening effect (the first row of indentations 10 μm from the surface had a slightly lower hardness but these were indents were too close to the surface) This result is in agreement with Fig. 5b: it was evident that no localized deformation or work hardening layer was present around the scribe and all of the material had been displaced during cutting.

Hardness profiles below the scratch roots were also measured (figure 9). For tool A scratches, a hardened region extending 100 μm was present below the scratch root. This layer was constant for every scratch and it did not change with the depth of the scratch, as shown in Figure 9a. The hardness was a maximum at the scratch root, and decreased continuously up to ~100 μm distance. This hardening can be attributed to the plastic deformation ahead of the scratch root, and this plastic deformation and the associated hardening plays a positive role in terms of the final fatigue life.

For tool B scratches, there was little evidence of any hardening at all below the scratch root, with perhaps a small hardness increase in the first 25 μm (figure 9b). The conclusion for tool B was that it removed material through a cutting mechanism that did not cause significant plastic work hardening around the tool flanks or below the root of the scratch it produced.

4.2.2 Clad material

The hardness maps obtained for the clad samples were also independent of the scratch depth, so results of only the 100 μm deep scratches are presented here. A similar scheme of indentations was performed as for the unclad Al 2024-T351. For tool A, the hardness values increased overall as the distance from the surface increased (figure 10a). The first row was again slightly too close to the surface for complete validity, and the third row of indentations straddled the interface between the clad and the substrate and an intermediate value of hardness was obtained. The final rows of indentations were located in the 2024 substrate region and these rows of indentations revealed a similar hardness behavior as for the unclad sample, indicating a localized hardening.

For tool B, no localized hardening effect was found near the scratches (Figure 10b).

The hardness below the notch roots for 100 μm scratches from each tool is shown in figure 11. For tool A, as for the scratches in the unclad material, a 100 μm layer was found in which the hardness was increased as much as 35% (figure 11a). The hardness then decreased continuously until it reached the parent material hardness after ~100 μm. For the tool B scratch, there was no hardening effect at the scratch root.

4.3 Diffraction peak widths

Figures 12a and 12b show diffraction peak widths obtained at the ESRF for scratches made by tool A and tool B in the 5091 aluminium. For the tool A scratch, a heavily-deformed

region was observed, which is asymmetric around the scratch and where the highest deformation was observed on the side of the tool that showed a defect in the scratch profile. For the tool B scratch, no such heavily deformed region was observed around the scratch, with only a very small increase in the peak width observed in a small region near the scratch root.

4.4 Fatigue testing

The fatigue lives of the samples scratched with the two tools to various scratch depths are shown in Table 2, and presented in Figure 13. In general, the fatigue life of the samples with scratches made with tool A are substantially higher than the fatigue life when using tool B. The exception is the 50 μm scratch made in the clad sample with tool A, which has an anomalously low life, although this has been observed previously for scratches within the clad layer that do not penetrate to the base metal. The higher fatigue life for tool A is attributed to the extensive plastic deformation and hardening associated with scratches made with this tool

Several samples were fatigue loaded without being taken to failure, in order to observe the effects of cyclic loading on the hardness at the scratch tip. Figure 12 shows typical results that were obtained. No change in the hardness at the scratch root was seen in either clad or unclad material, for scratches produced with either tool.

It is therefore likely that the initial state of the material after the scratch is produced, in terms of the local hardness and residual stress, is not further affected by fatigue loading to a significant degree.

Conclusions

1. Nanoindentation has been used to map the hardness around scratches in clad and unclad 2024 aluminium alloy, for scratches produced with two different tools. The hardening around such features is extremely localized and a method is required with a very high spatial resolution in order to be able to discern the small-scale changes that are induced.

2. The two tools studied produced very different scratch profiles. Tool A was less ‘sharp’, and appeared to have some damage on the tool profile. Tool A produced a scratch by a ploughing rather than a cutting mechanism, and examination of the scratches it produced indicated that its attack angle was probably greater than for tool B. A higher attack angle is expected to tend towards ploughing during the production of a scratch.

3. Tool A showed significant hardening around the scratch, which was not seen for the sharper tool B. The hardening was correlated with results from synchrotron X-ray diffraction, which showed greater peak broadening (indicative of a higher degree of plastic damage) around the scratch from tool A, and also an asymmetry in the peak broadening associated with the damage on the tool profile.

4. No change in the local hardness around the scratch was observed with fatigue loading of samples containing scratches.

Acknowledgements

Mr I. Norman of Materials Engineering at The Open University is thanked for his help with the experimental work. Dr. A. Evans is thanked for his assistance with the experiment on ID31 at the ESRF. MKK is funded by Airbus Deutschland, and Dr D. Furfari is duly acknowledged for his support. MEF is supported by a grant through The Open University from the Lloyd's Register Educational Trust, an independent charity working to achieve advances in transportation, science, engineering and technology education, training and research worldwide for the benefit of all.

References

[1] Y. M. Chen, L. K. Ives and J. W. Dally, Numerical simulation of sliding contact over a half-plane, Wear. 185 (1995) 83-91.

[2] J. H. Lee, G. H. Xu and H. Liang, Experimental and numerical analysis of friction and wear behavior of polycarbonate, Wear. 251 (2001) 1541-1556.

[3] Y. H. Lee and D. Kwon, Measurement of residual-stress effect by nanoindentation on elastically strained (100) W, Scripta Materialia. 49 (2003) 459-465.

[4] Y. H. Lee, K. Takashima and D. Kwon, Micromechanical analysis on residual stress-induced nanoindentation depth shifts in DLC films, Scripta Materialia. 50 (2004) 1193-1198.

[5] S. Suresh and A. E. Giannakopoulos, A new method for estimating residual stresses by instrumented sharp indentation, Acta Materialia. 46 (1998) 5755-5767.

[6] Z.-H. Xu and X. Li, Influence of equi-biaxial residual stress on unloading behaviour of nanoindentation, Acta Materialia. 53 (2005) 1913-1919.

[7] Z. H. Xu and X. Li, Estimation of residual stresses from elastic recovery of nanoindentation, Philosophical Magazine. 86 (2006) 2835-2846.

[8] W. C. Oliver and G. M. Pharr, An improved technique for determining hardness and elastic modulus using load and displacement sensing indentation experiments, J. Mater. Res. 7 (1992) 1564-1583.

[9] G. M. Pharr, W. C. Oliver and F. R. Brotzen, On the generality of the relationship among contact stiffness, contact area, and elastic modulus during indentation, J. Mater. Res. 7 (1992) 613-617.

[10] M. K. Khan, S. V. Hainsworth, M. E. Fitzpatrick and L. Edwards, Application of the work of indentation approach for the characterization of aluminium 2024-T351 and Al cladding by nanoindentation, J. Mater. Sci. 44 (2009) 1006-1015.

[11] J. M. Sprauel, in M. E. Fitzpatrick and A. Lodini (eds.), *Analysis of residual stress by diffraction using neutron and synchrotron radiation*, Taylor and Francis, London, UK, 2003, p. 78-96.

[12] M. E. Fitzpatrick, M. T. Hutchings and P. J. Withers, Separation of Measured Fatigue Crack Stress Fields in a Metal Matrix Composite Material, Acta Mater. 47 (1999) 585-593.

[13] S. Mezlini, P. Kapsa, C. Henon and J. Guillement, Abrasion of aluminium alloy: effect of subsurface hardness and scratch interaction simulation, Wear. 257 (2004) 892-900.

[14] K. Kato, Micro-mechanisms of wear -- wear modes, Wear. 153 (1992) 277-295.

[15] C. Subramanian, Some considerations towards the design of a wear resistant aluminium alloy, Wear. 155 (1992) 193-205.

[16] M. Ben Tkaya, M. Zidi, S. Mezlini and P. Kapsa, Influence of the attack angle on the scratch testing of an aluminium alloy by cones: Experimental and numerical studies, Materials & Design. 29 (2008) 98-104.

Figure captions

Figure 1: Load:displacement curve produced during a single indentation

Figure 2. Sectional view of Al2024-T351 Clad Plate

Figure 3. Grain Size Determination (a) Secondary electron image (b) EBSD image

Figure 4: Scratch geometry

Figure 5: SEM images of the scratch cross-section from (a) tool A (b) tool B

Figure 6: Indentation map

Figure 7: Surface Profile of scratches in clad Al2024-T351 a) 50 µm from tool A b) 50 µm from tool B

Figure 8: (a) Hardness values in unclad Al2024-T351 around a 75 µm scratch from tool A; (b) Hardness around a 100 µm scribe from Tool B

Figure 9: Hardness below the root of scratches in Al 2024-T351 from (a) tool A; (b) tool B

Figure 10: (a) Hardness values in clad Al2024-T351 around a 100 µm scratch from tool A; (b) Hardness around a 100 µm scribe from Tool B

Figure 11: Hardness below the root of 100 µm scratches in the clad Al 2024-T351 from (a) tool A; (b) tool B

Figure 12: Peak widths, expressed as degree spread of the full-width at half-maximum of the diffraction peak, around scratches made by a) Tool A; b) Tool B

Figure 13: Fatigue lives obtained from scratches made to different depths with the two different tools

Figure 14: Hardness below the scratch toot after fatigue (a) in unclad Al2024-T351 from a 100 µm scratch from tool A; (b) in clad Al2024-T351 from a 100 µm deep scratch from tool B

Material	E / GPa	σ_y / MPa	Hardness / GPa	E / σ_y	Strain Hardening coefficient
Al-Cladding	69	110	0.45	627	0.2
Al 2024-T351	73	360	1.75	203	0.13

Table 1: Mechanical property data for Al-Clad and Al2024-T351.

Test #	Clad/Unclad	Tool	Depth / μm	Radius / μm	Fatigue Life / No. of cycles
1	U	A	50	5	923338
2	U	A	75	5	887359
3	U	A	100	5	841586
4	U	B	50	5	112140
5	U	B	100	5	80851
6	C	A	50	5	227747
7	C	B	50	5	13700
8	C	B	100	5	135028
9	C	A	100	5	914563

Table 2 Fatigue life of scratches in Four Point Bending

Figure 1

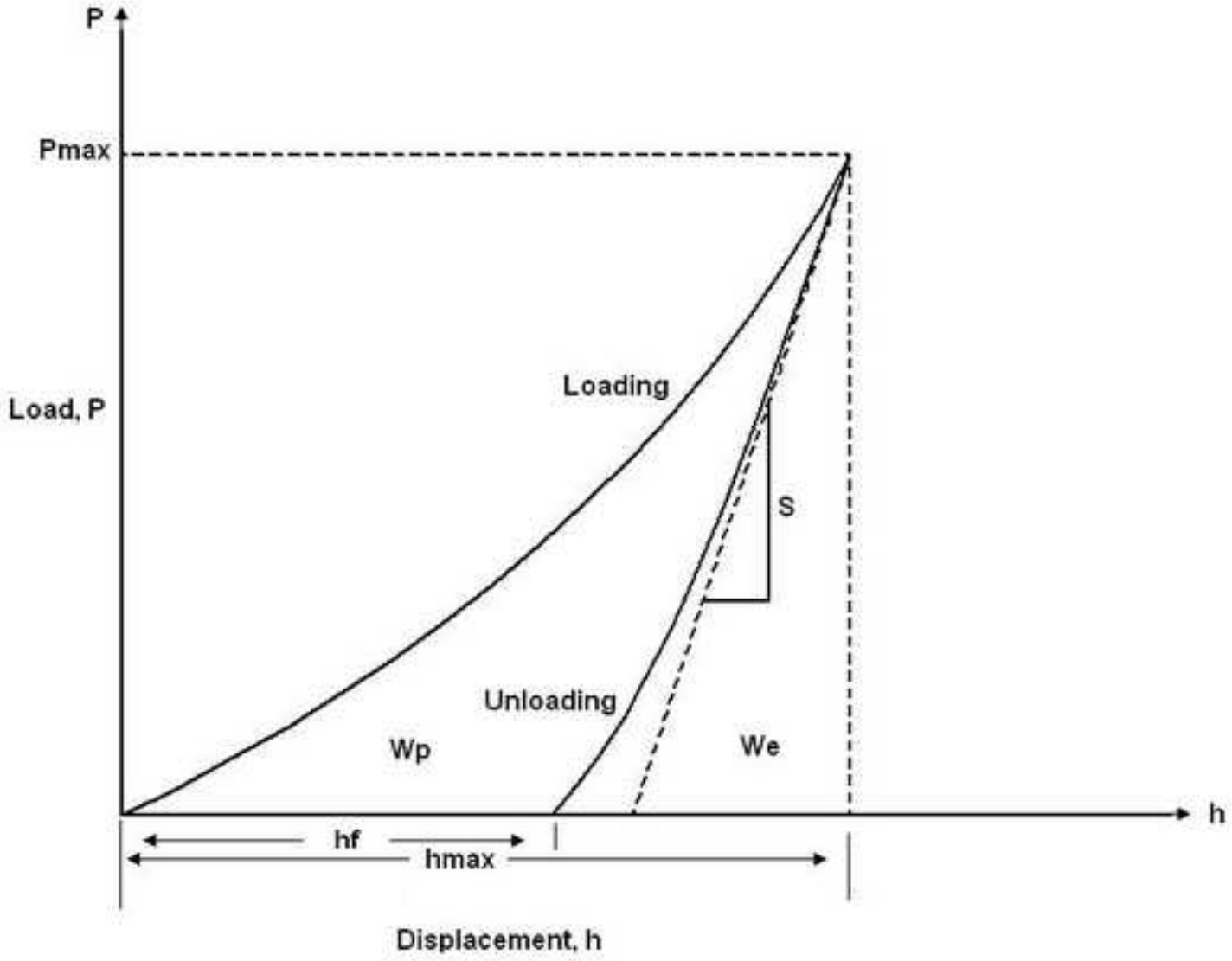
P
Pmax
Load, P
Loading
S
Unloading
Wp
We
h
hf
hmax
Displacement, h

Figure 2

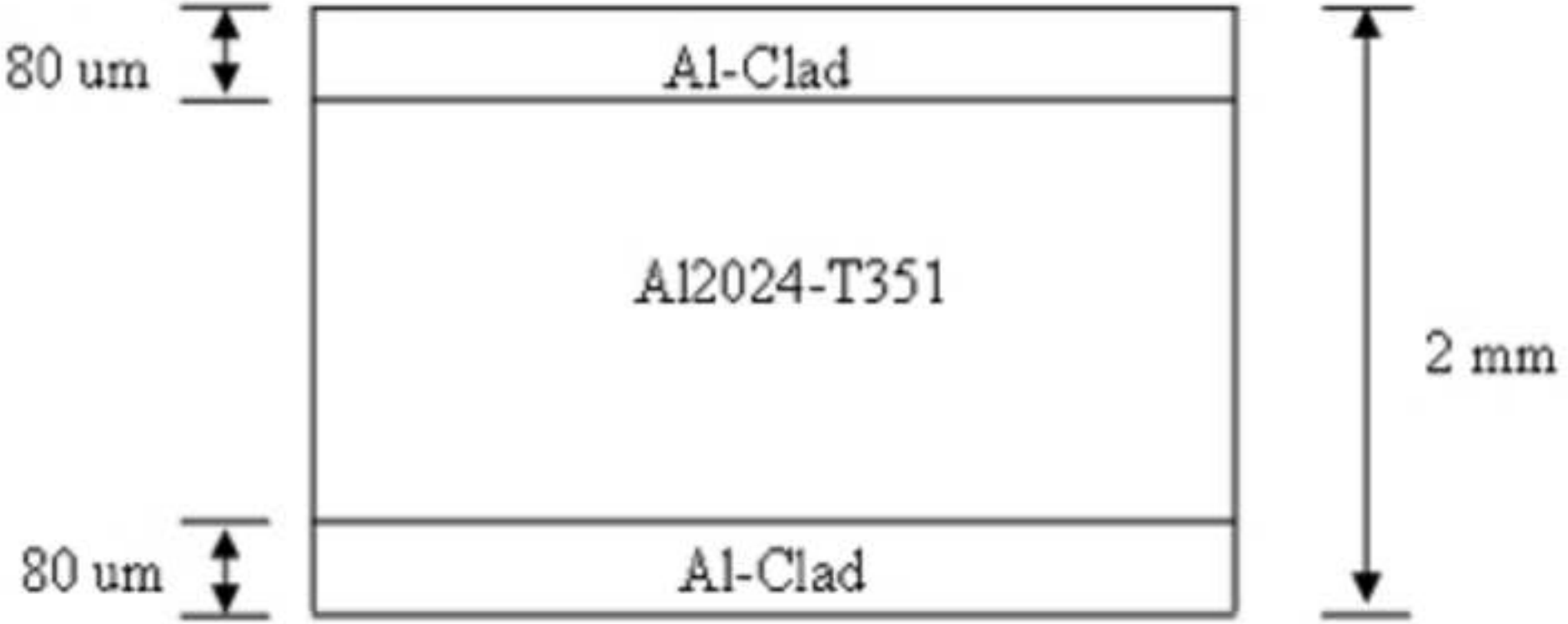

Figure 3a

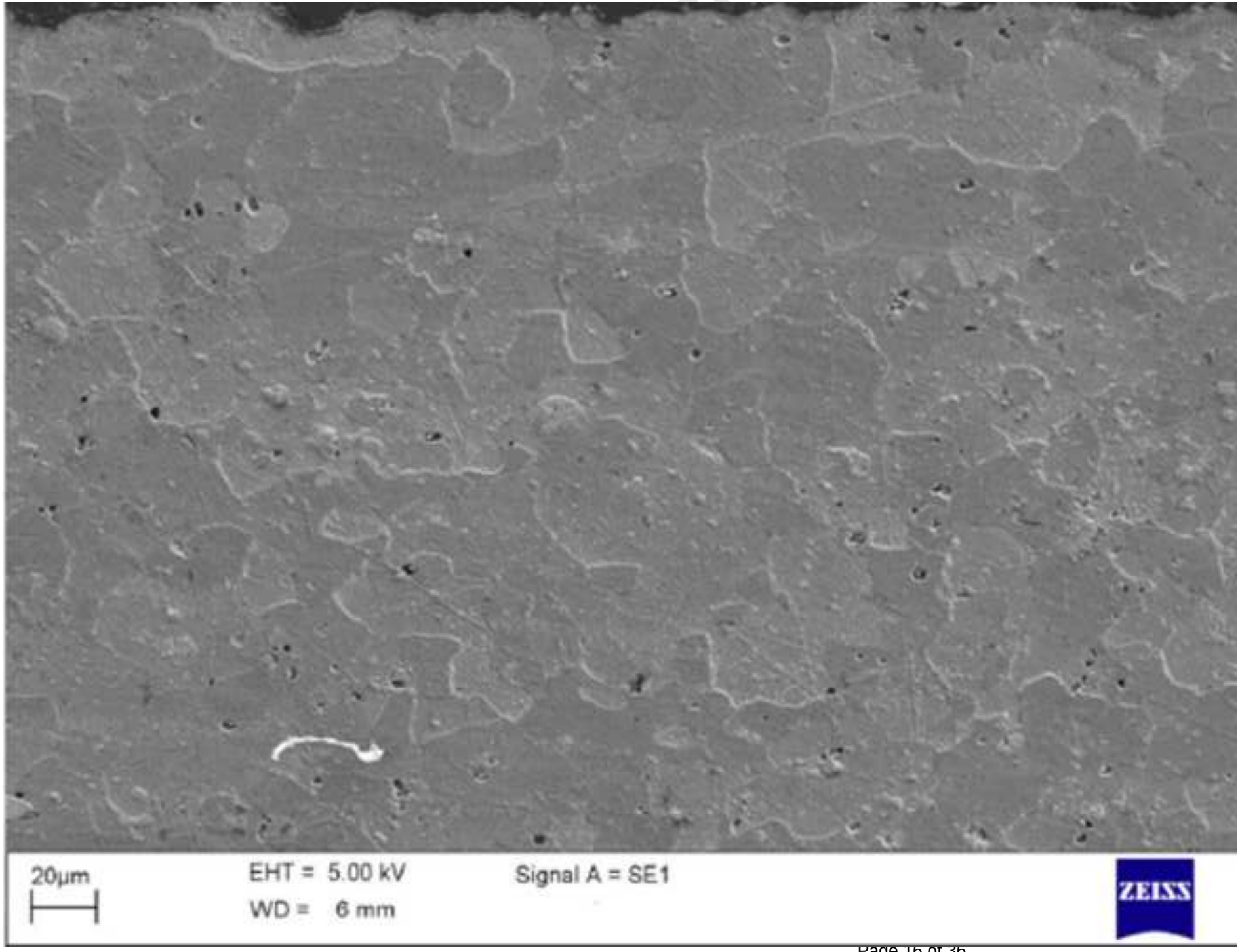

Figure 3b

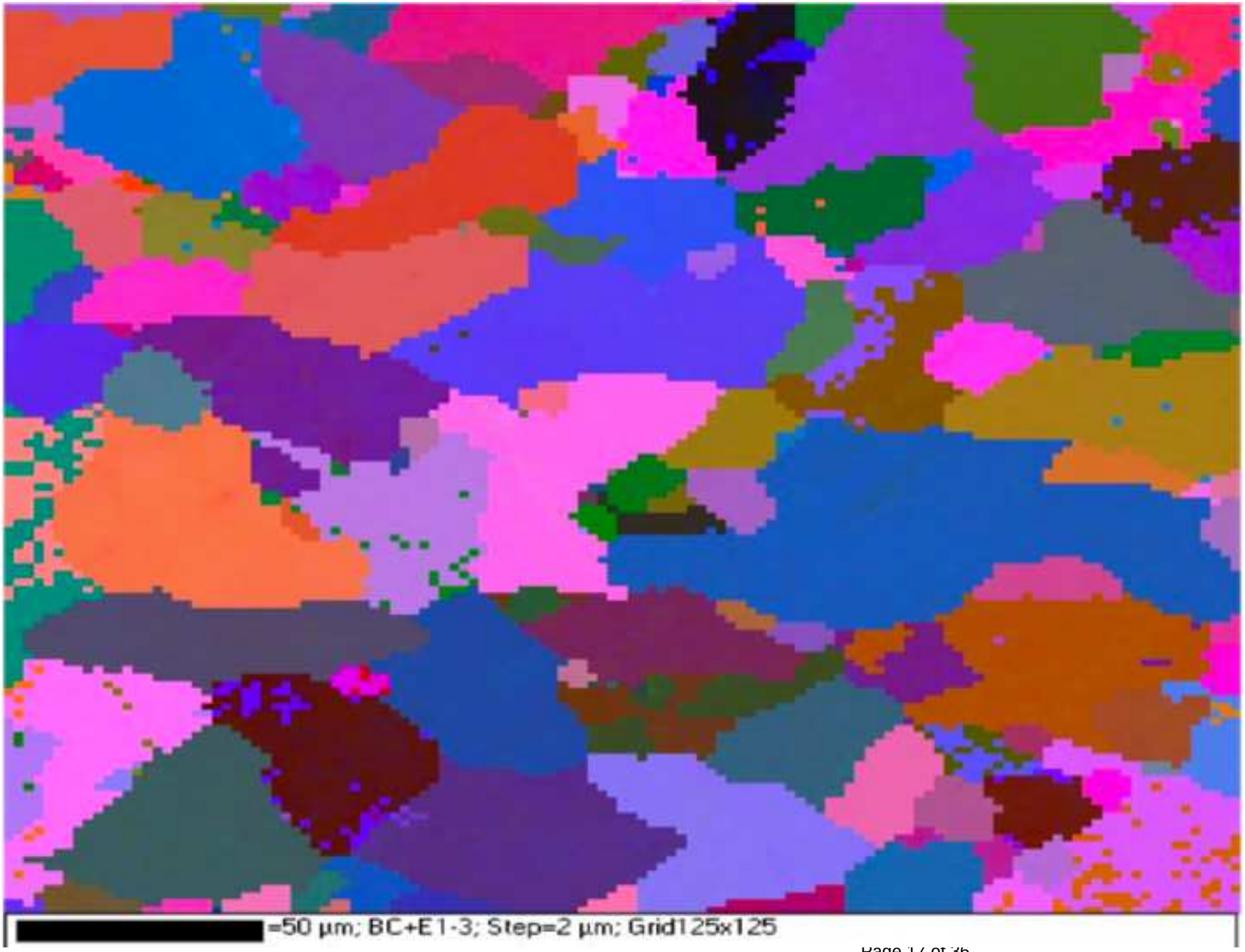

Figure 4

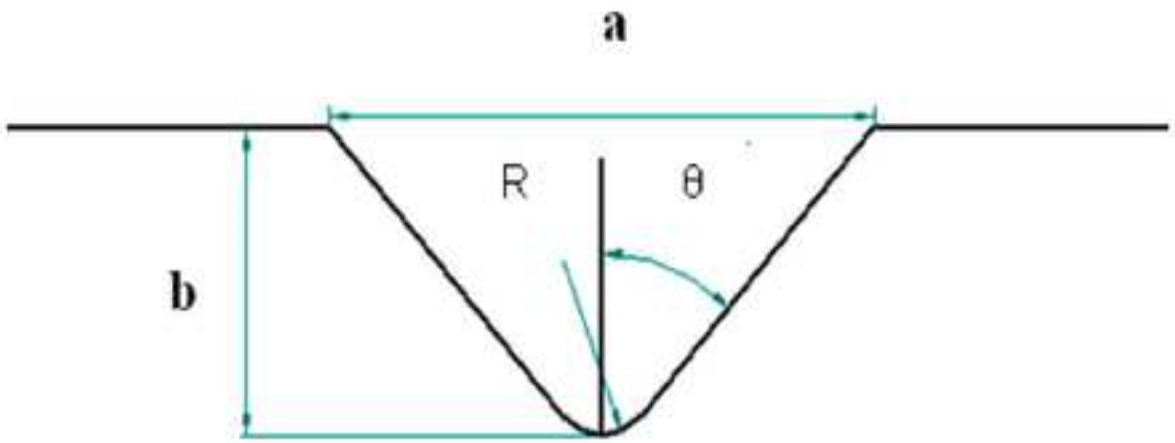

Figure 5a

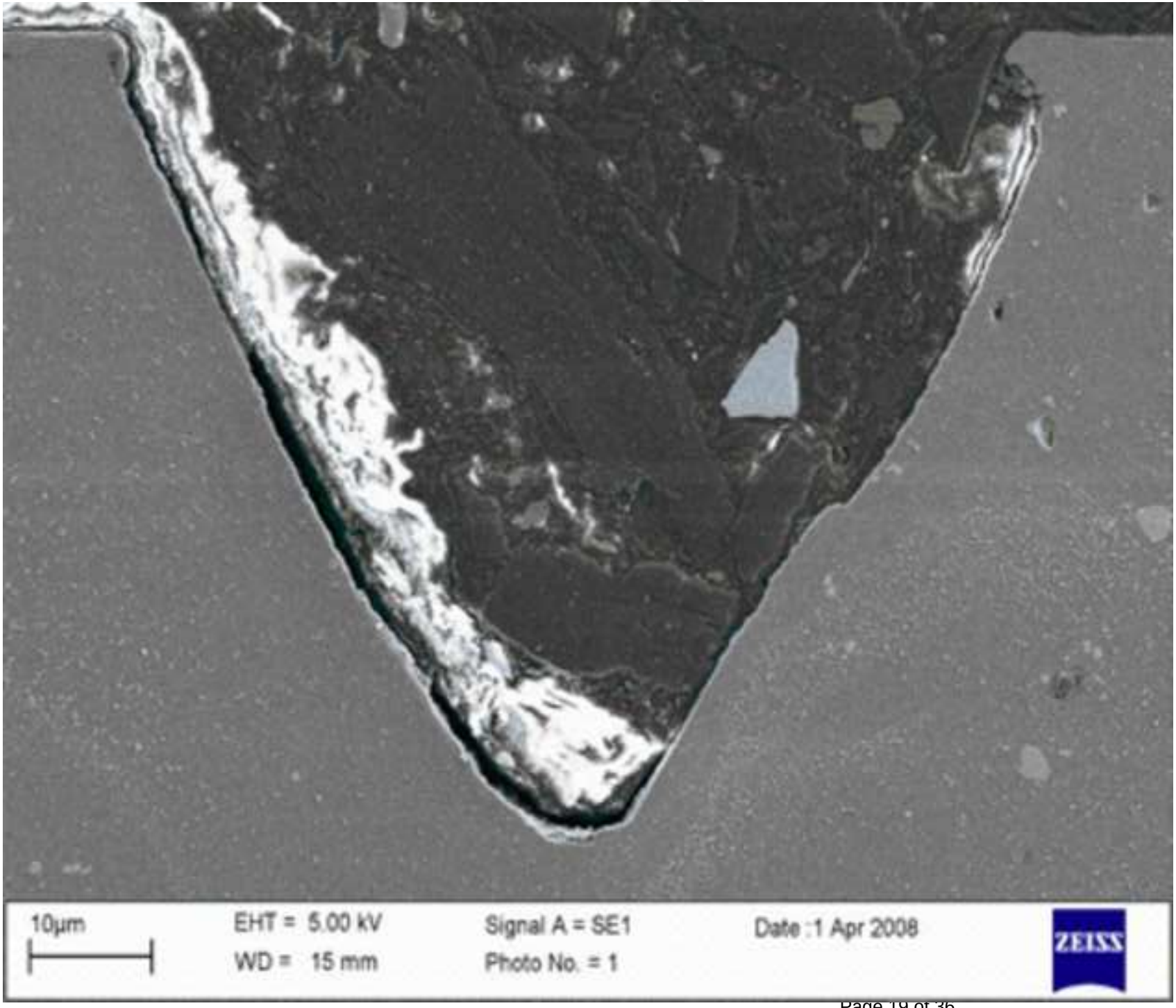
10µm
EHT = 5.00 kV
WD = 15 mm
Signal A = SE1
Photo No. = 1
Date :1 Apr 2008
ZEISS

Figure 5b

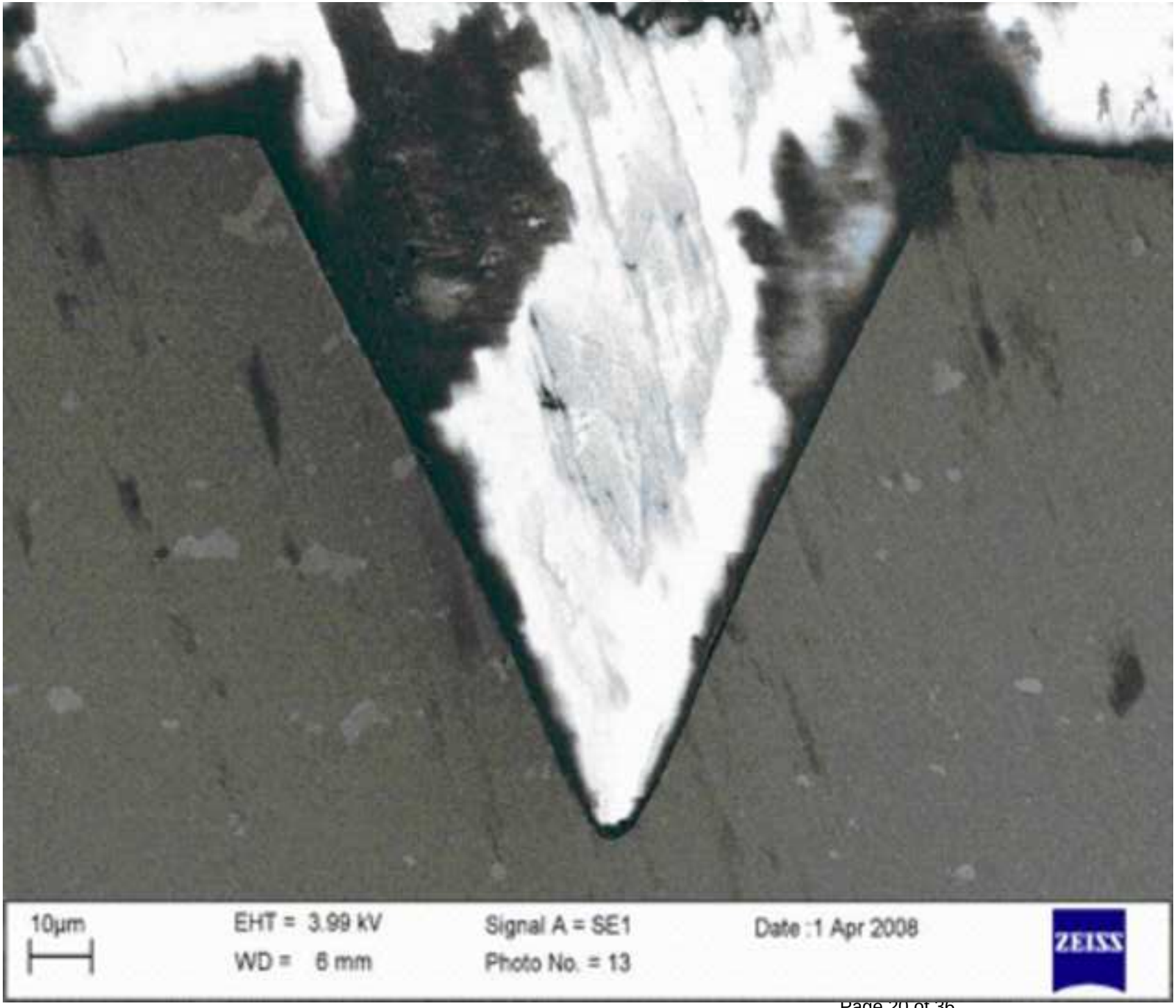
10µm
EHT = 3.99 kV
WD = 6 mm
Signal A = SE1
Photo No. = 13
Date :1 Apr 2008
ZEISS

Figure 6

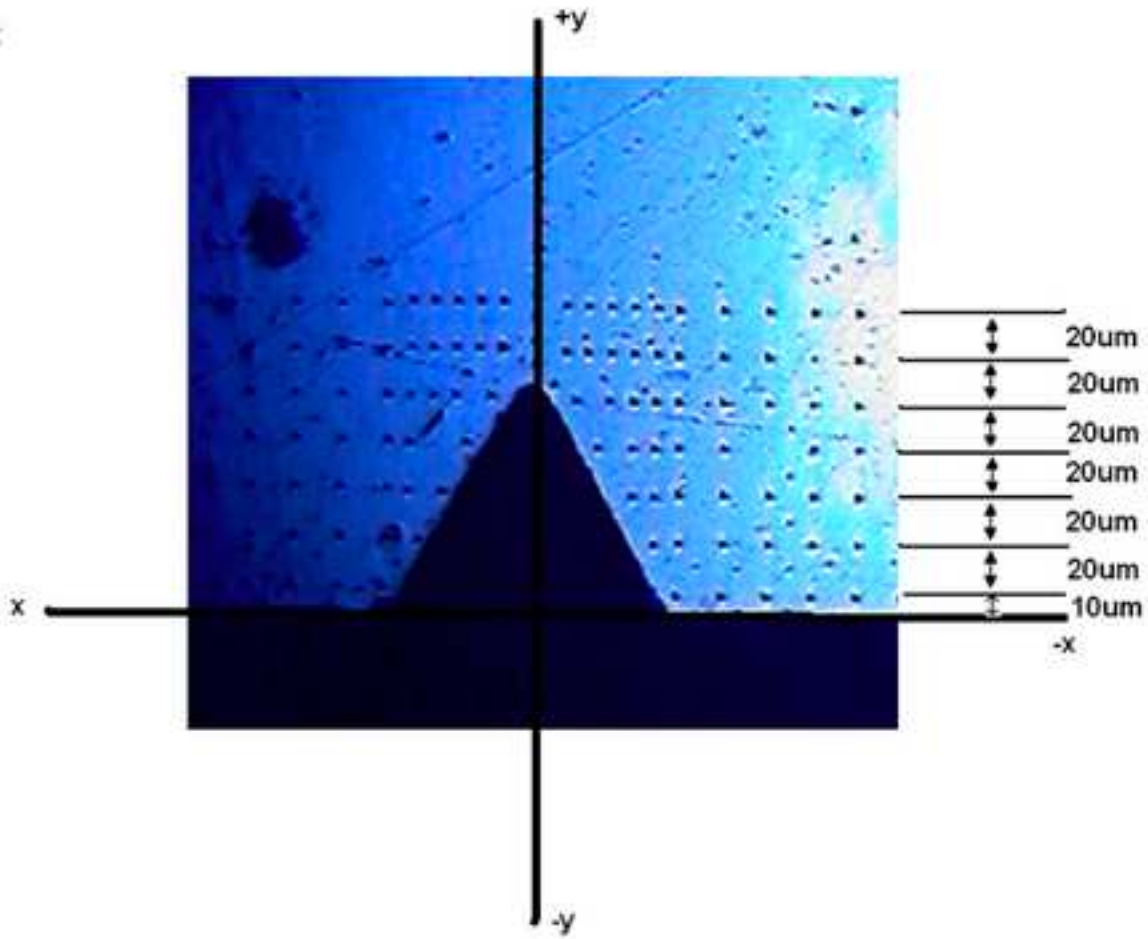

Figure 7a

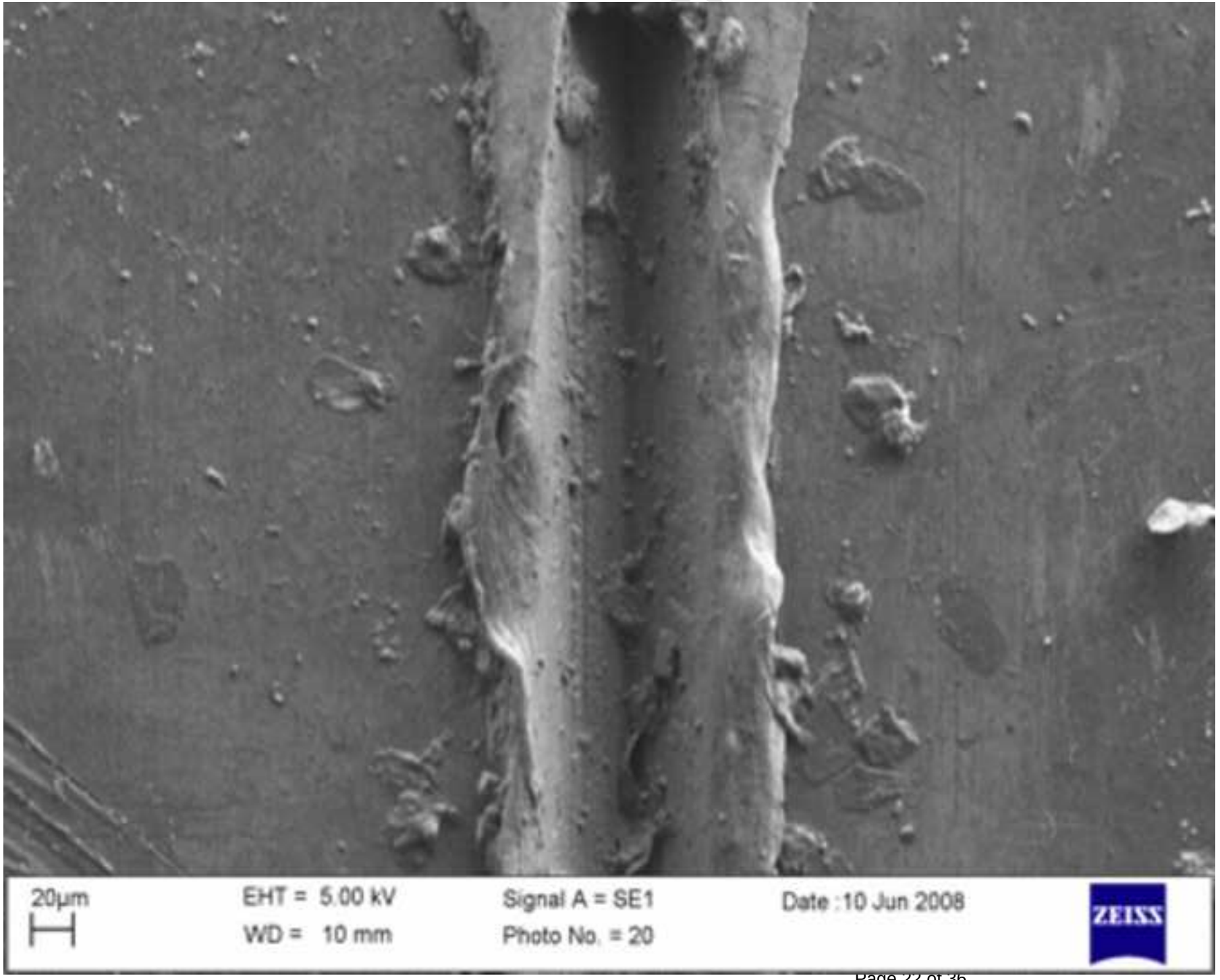
20µm
EHT = 5.00 kV
WD = 10 mm
Signal A = SE1
Photo No. = 20
Date :10 Jun 2008
ZEISS

Figure 7b

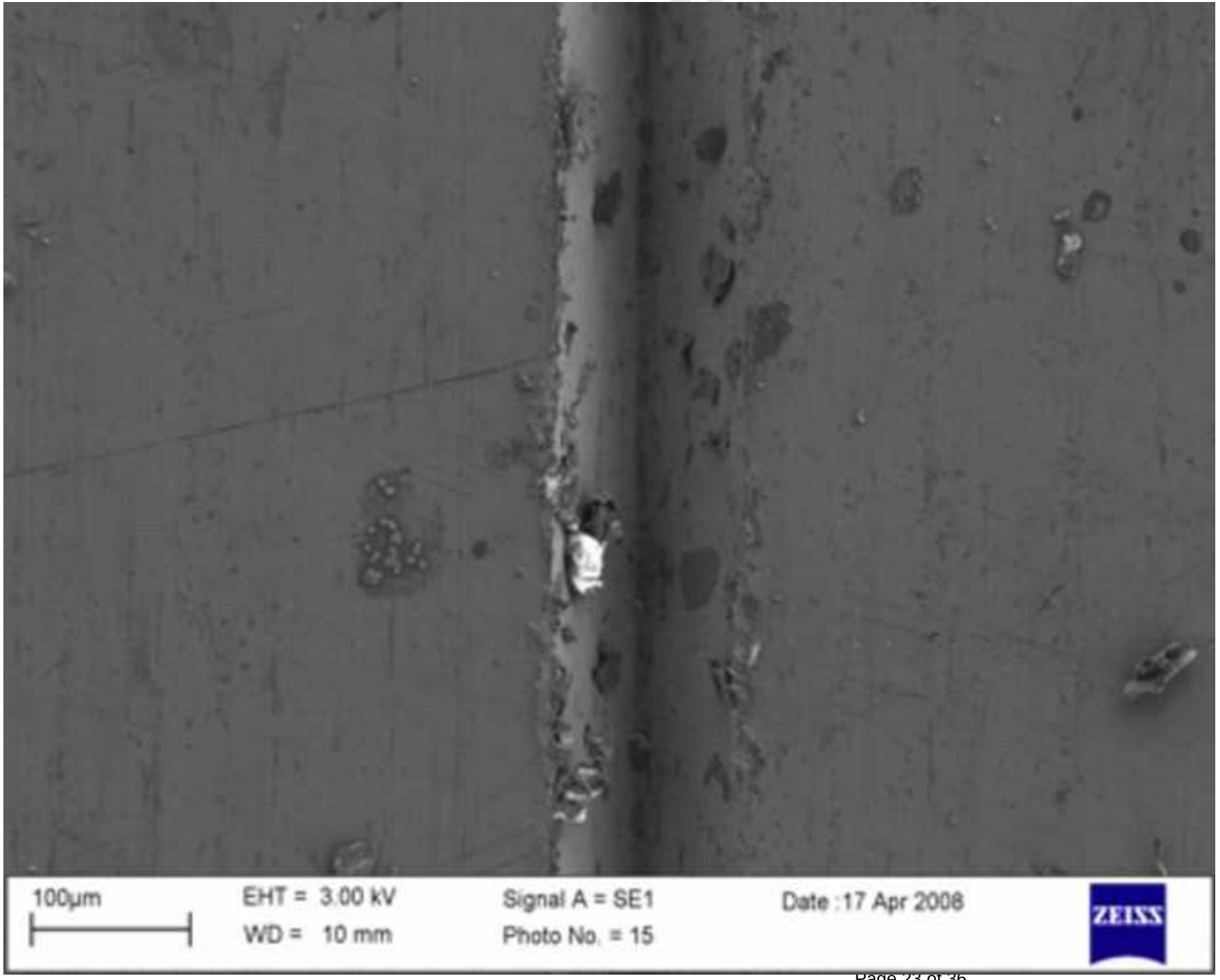
100µm
EHT = 3.00 kV
WD = 10 mm
Signal A = SE1
Photo No. = 15
Date :17 Apr 2008
ZEISS

Figure 8a

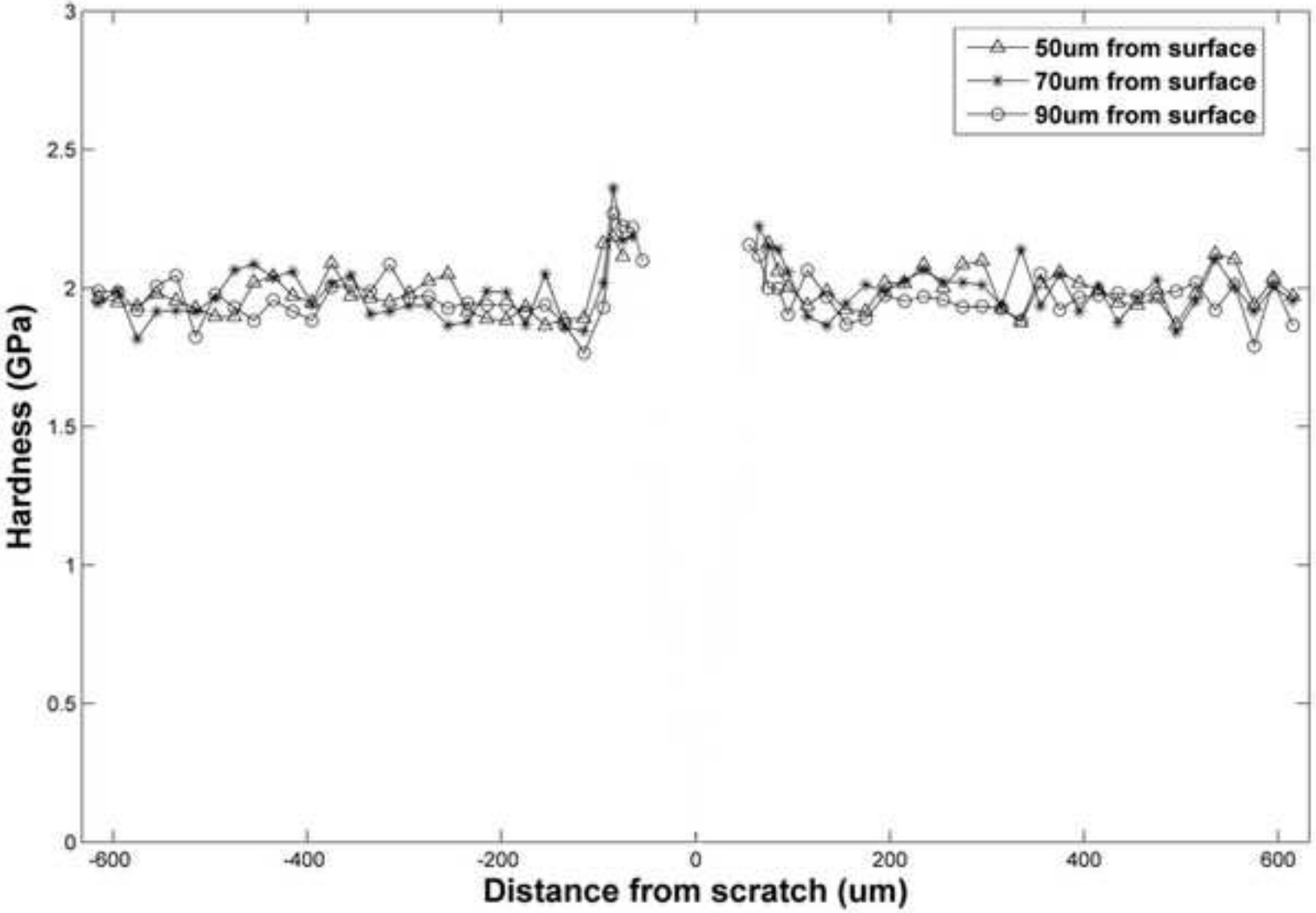
50um from surface
70um from surface
90um from surface
Hardness (GPa)
Distance from scratch (um)
0
0.5
1
1.5
2
2.5
3
-600
-400
-200
0
200
400
600

Figure 8b

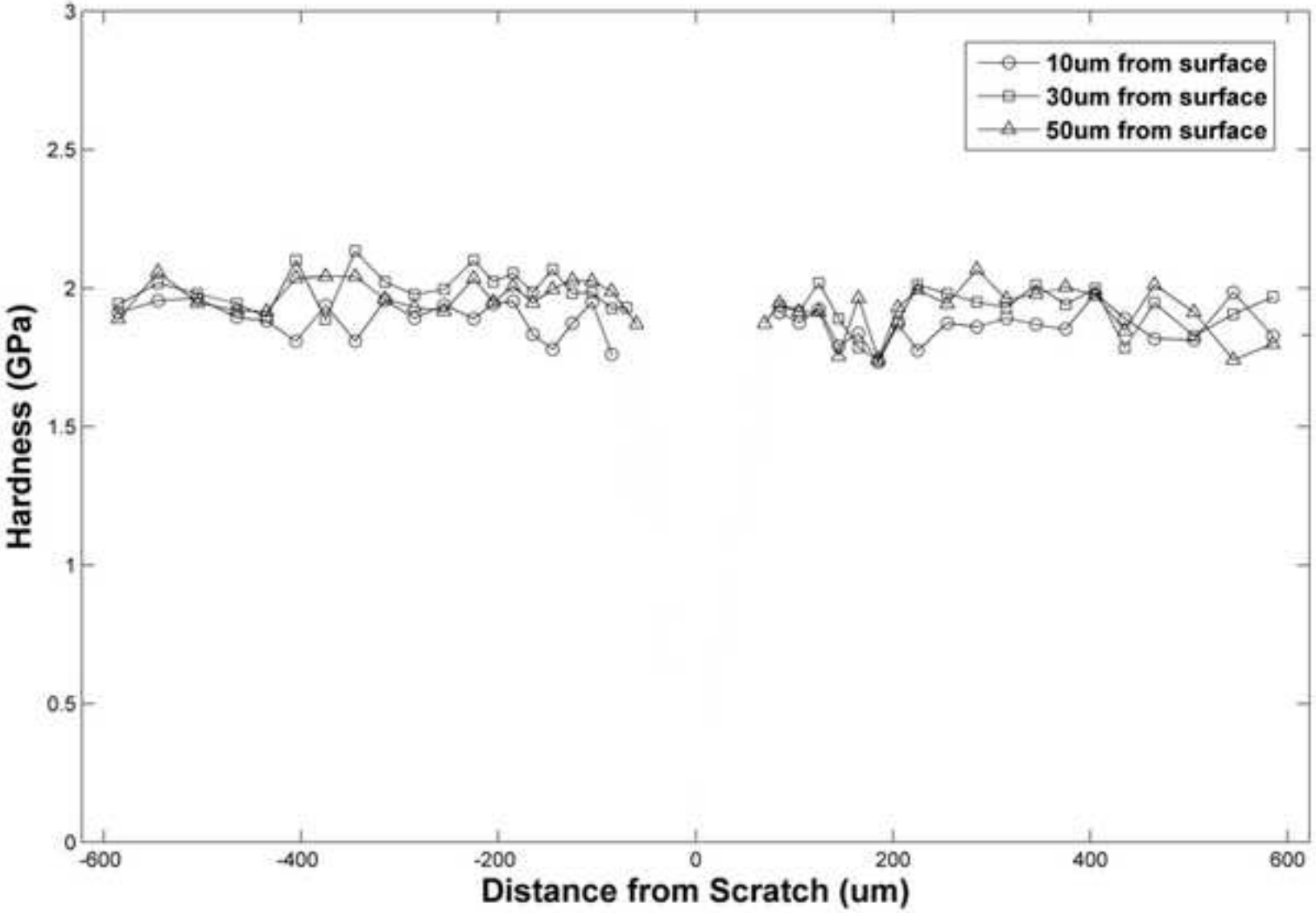
10um from surface
30um from surface
50um from surface
Hardness (GPa)
Distance from Scratch (um)
0
0.5
1
1.5
2
2.5
3
-600
-400
-200
0
200
400
600

Figure 9a

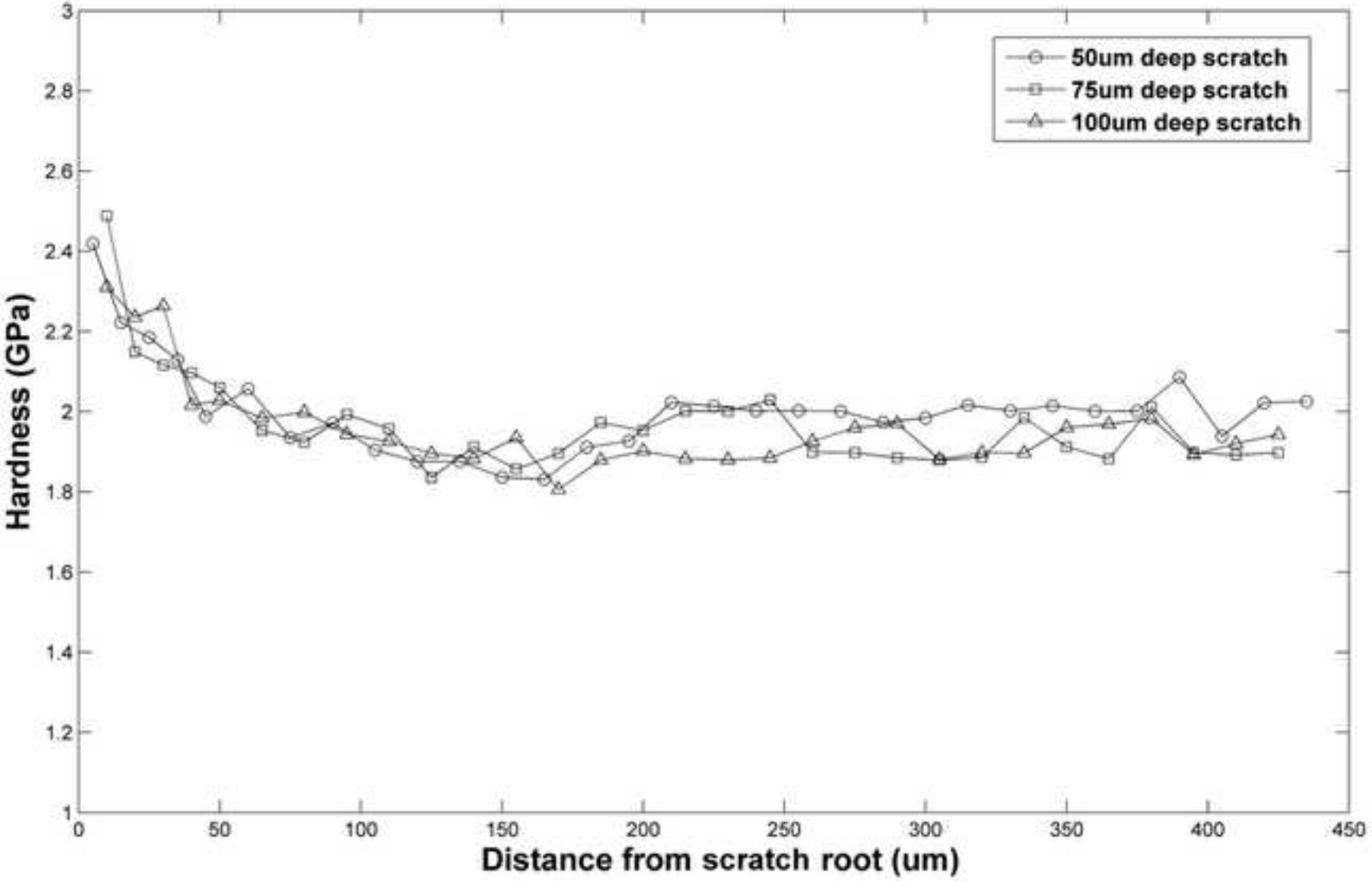
50um deep scratch
75um deep scratch
100um deep scratch
Hardness (GPa)
Distance from scratch root (um)
3
2.8
2.6
2.4
2.2
2
1.8
1.6
1.4
1.2
1
0
50
100
150
200
250
300
350
400
450

Figure 9b

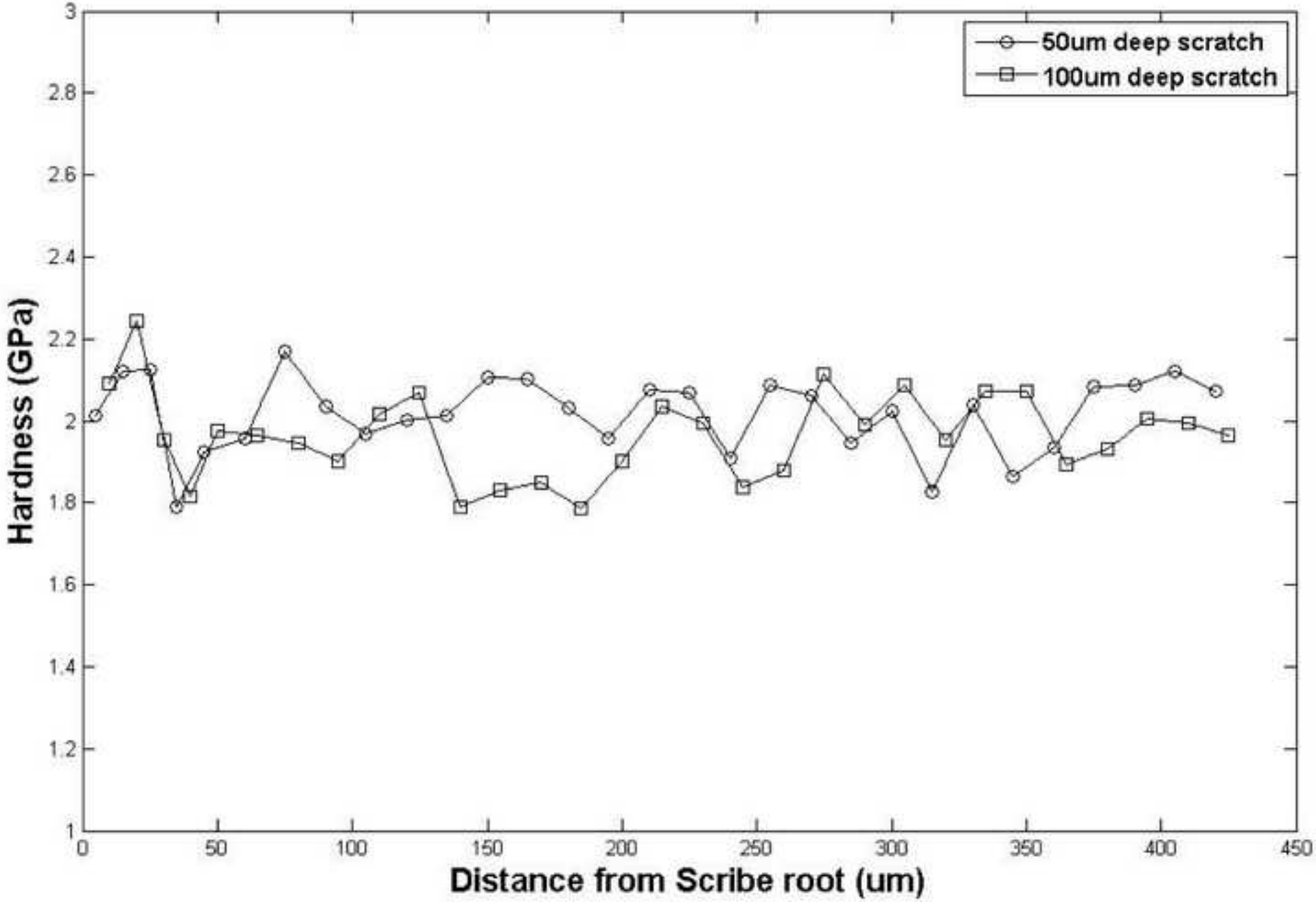
50um deep scratch
100um deep scratch
Hardness (GPa)
Distance from Scribe root (um)
3
2.8
2.6
2.4
2.2
2
1.8
1.6
1.4
1.2
1
0
50
100
150
200
250
300
350
400
450

Figure 10a

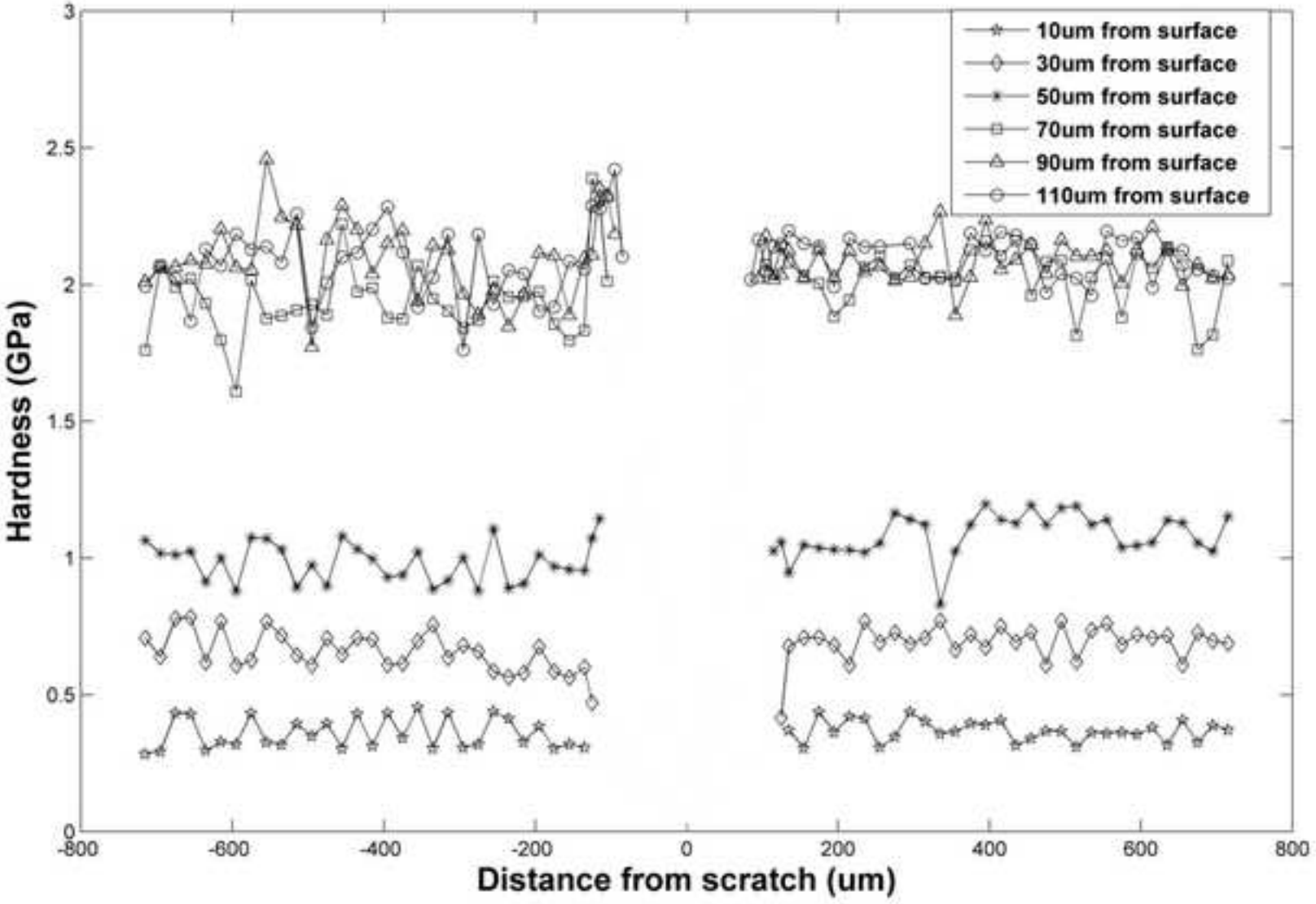
10um from surface
30um from surface
50um from surface
70um from surface
90um from surface
110um from surface
Hardness (GPa)
Distance from scratch (um)
0
0.5
1
1.5
2
2.5
3
-800
-600
-400
-200
0
200
400
600
800

Figure 10b

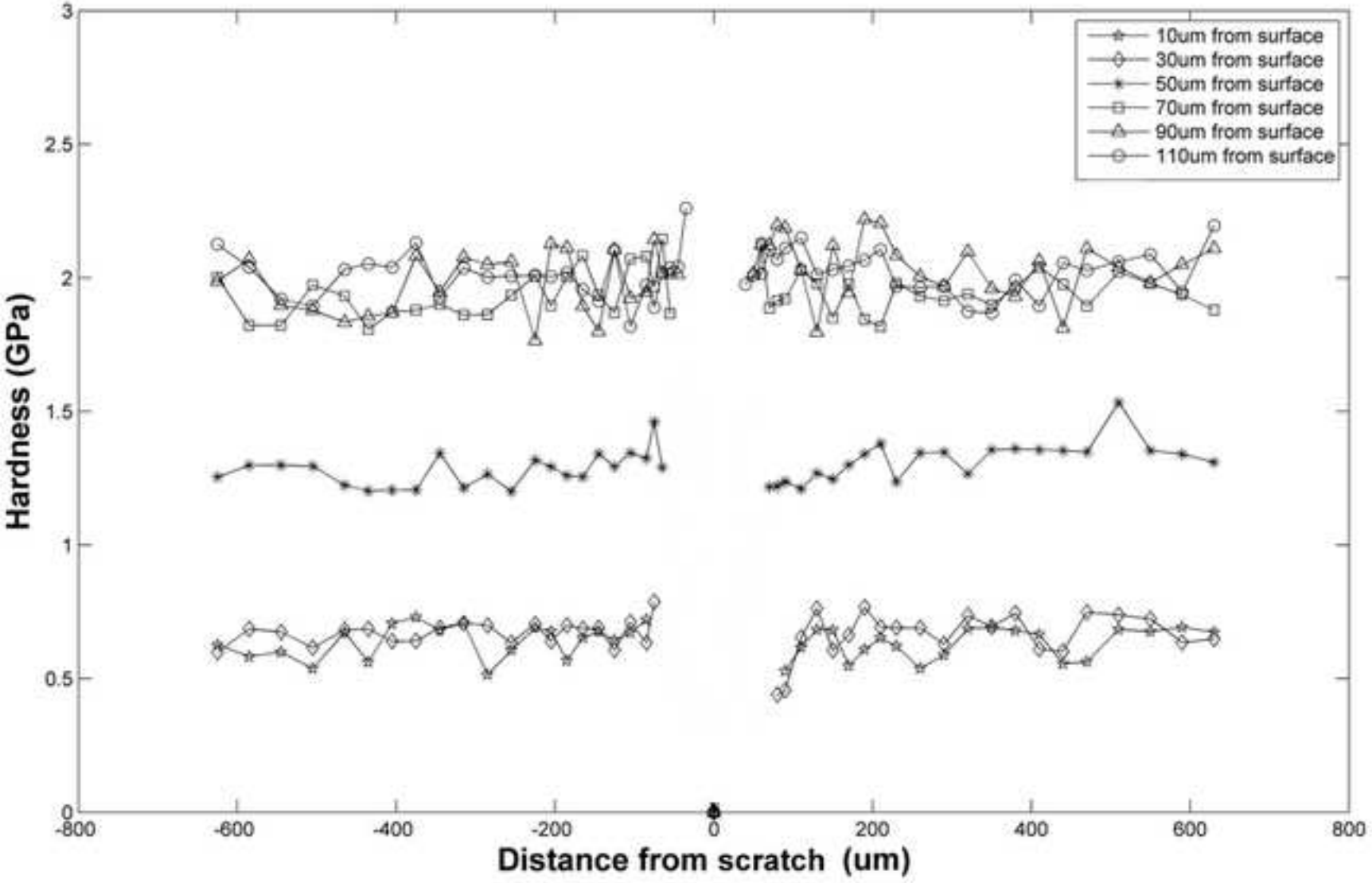
10um from surface
30um from surface
50um from surface
70um from surface
90um from surface
110um from surface
Hardness (GPa)
Distance from scratch (um)
3
2.5
2
1.5
1
0.5
0
-800
-600
-400
-200
0
200
400
600
800

Figure 11a

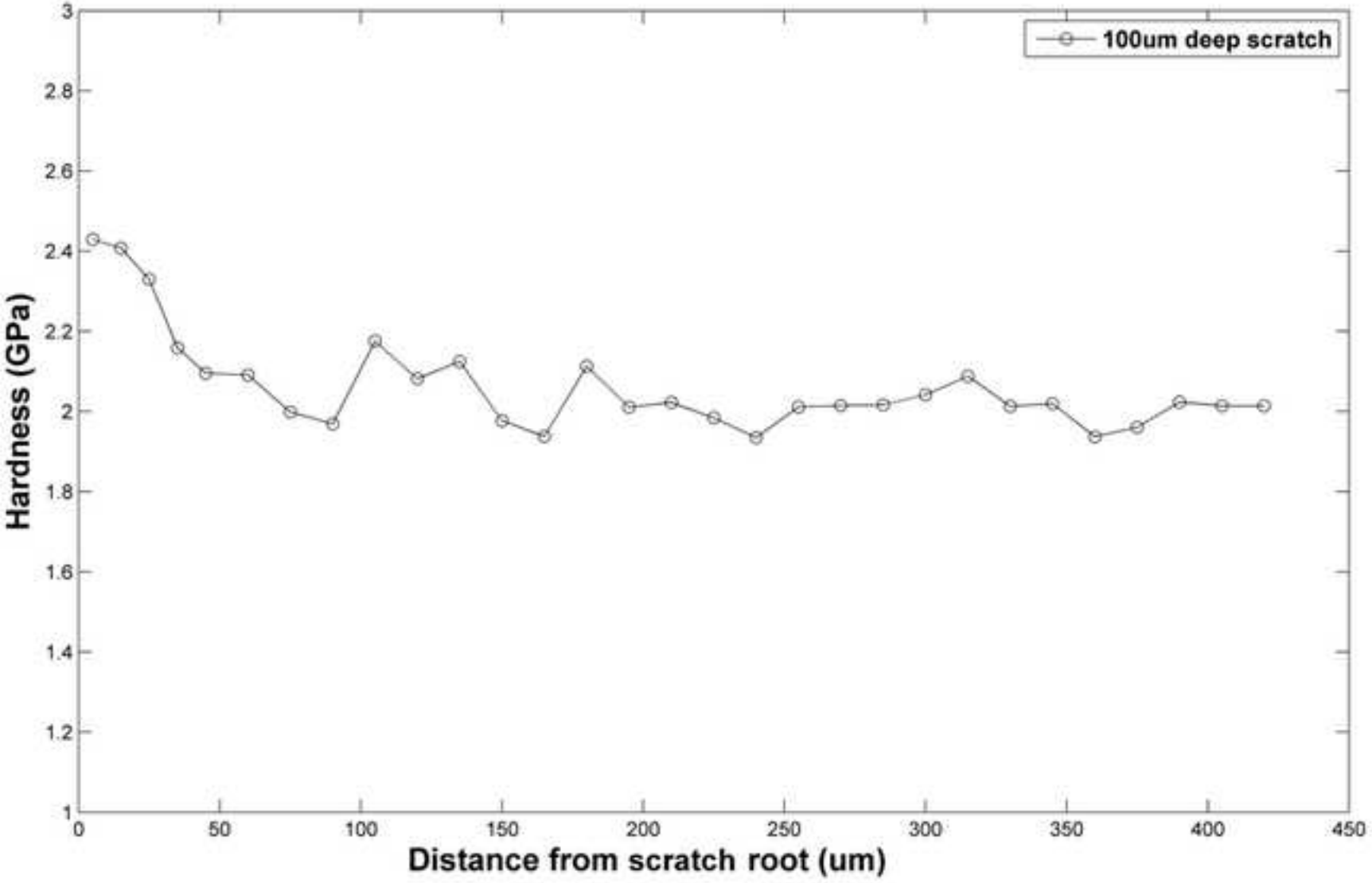
100um deep scratch
Hardness (GPa)
Distance from scratch root (um)
3
2.8
2.6
2.4
2.2
2
1.8
1.6
1.4
1.2
1
0
50
100
150
200
250
300
350
400
450

Figure 11b

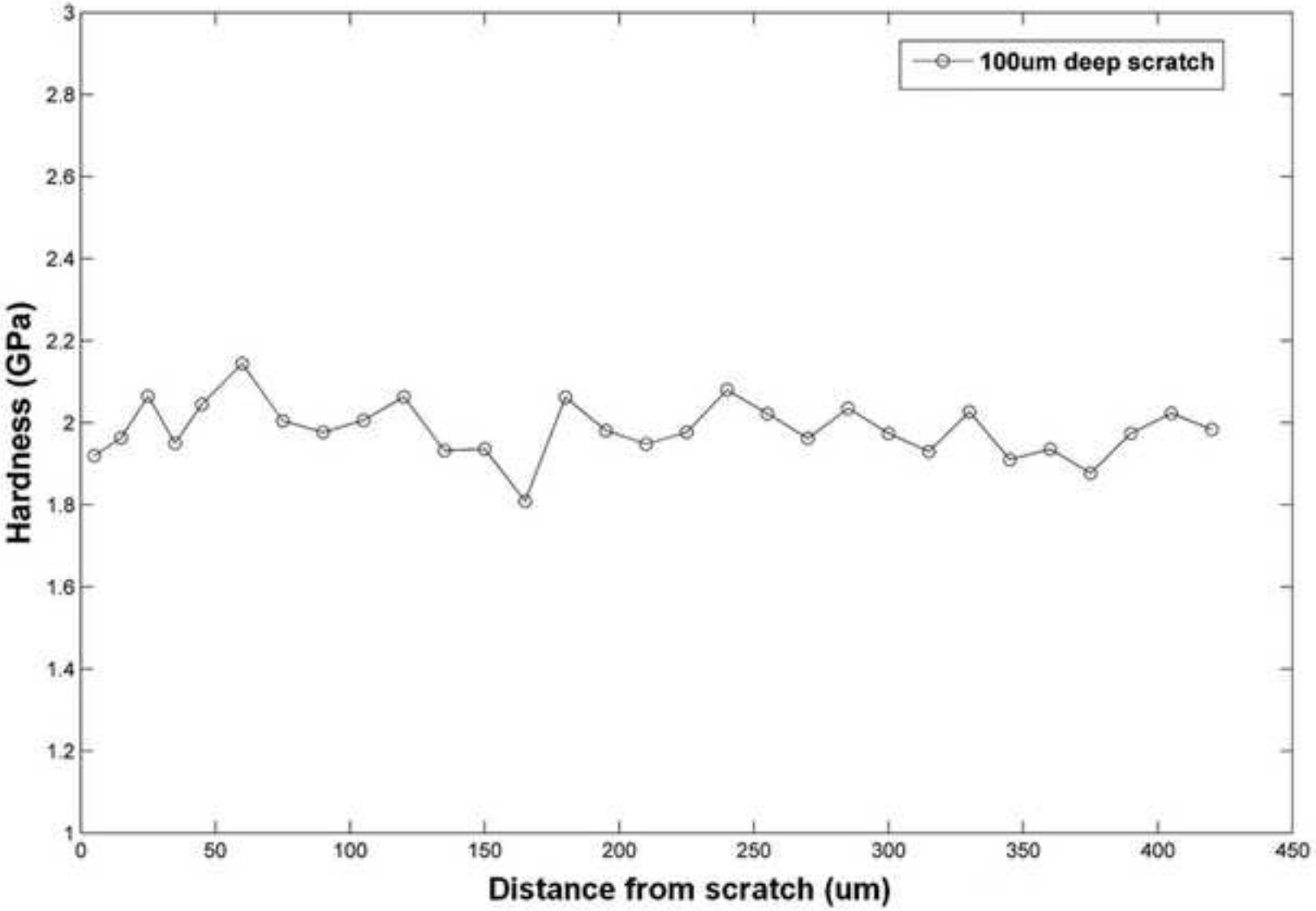
100um deep scratch
Hardness (GPa)
Distance from scratch (um)
3
2.8
2.6
2.4
2.2
2
1.8
1.6
1.4
1.2
1
0
50
100
150
200
250
300
350
400
450

Figure 12a

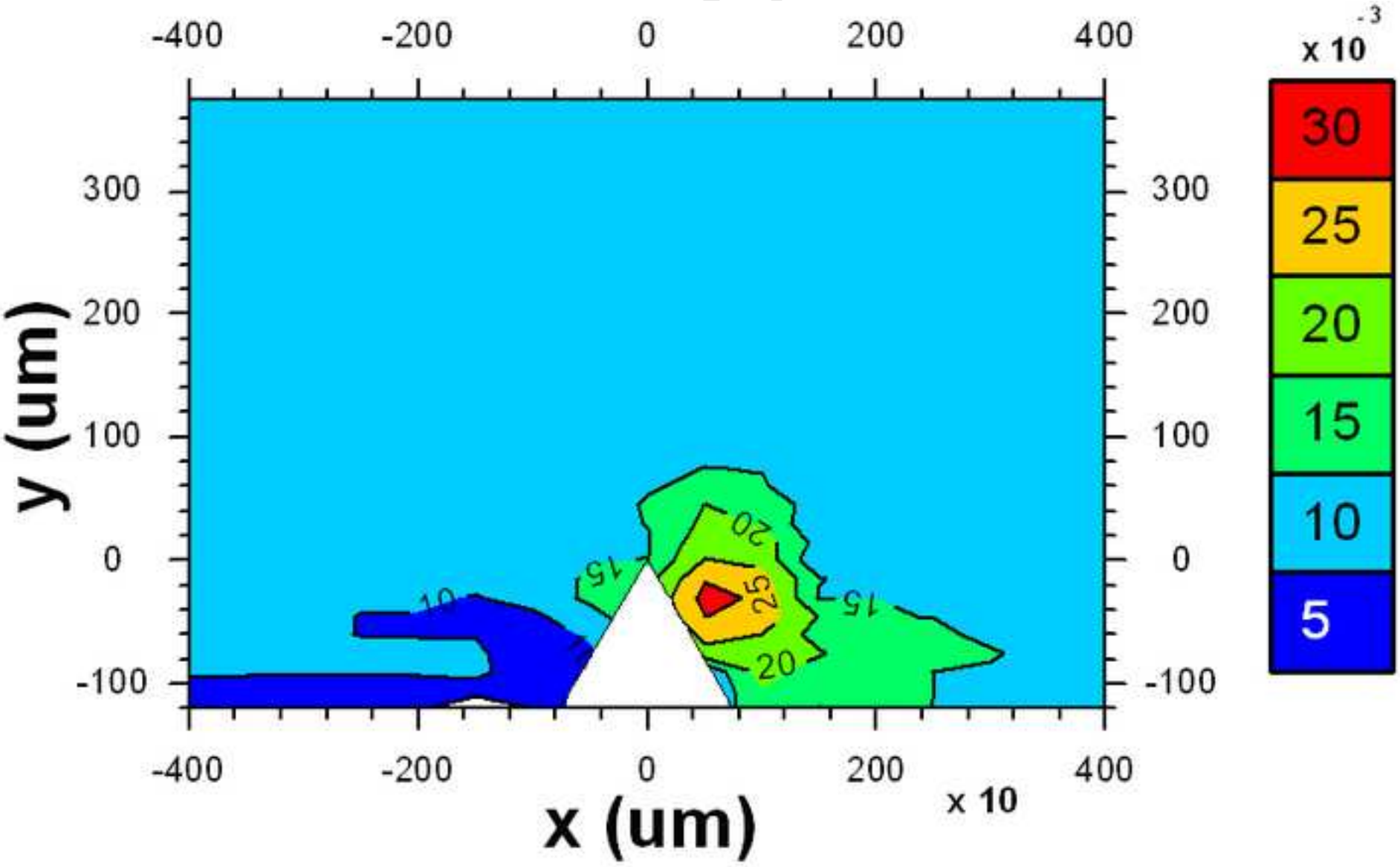
-400
-200
0
200
400
300
200
100
0
-100
y (um)
x (um)
x 10
x 10 -3
30
25
20
15
10
5
10
15
20
25
15
20

Figure 12b

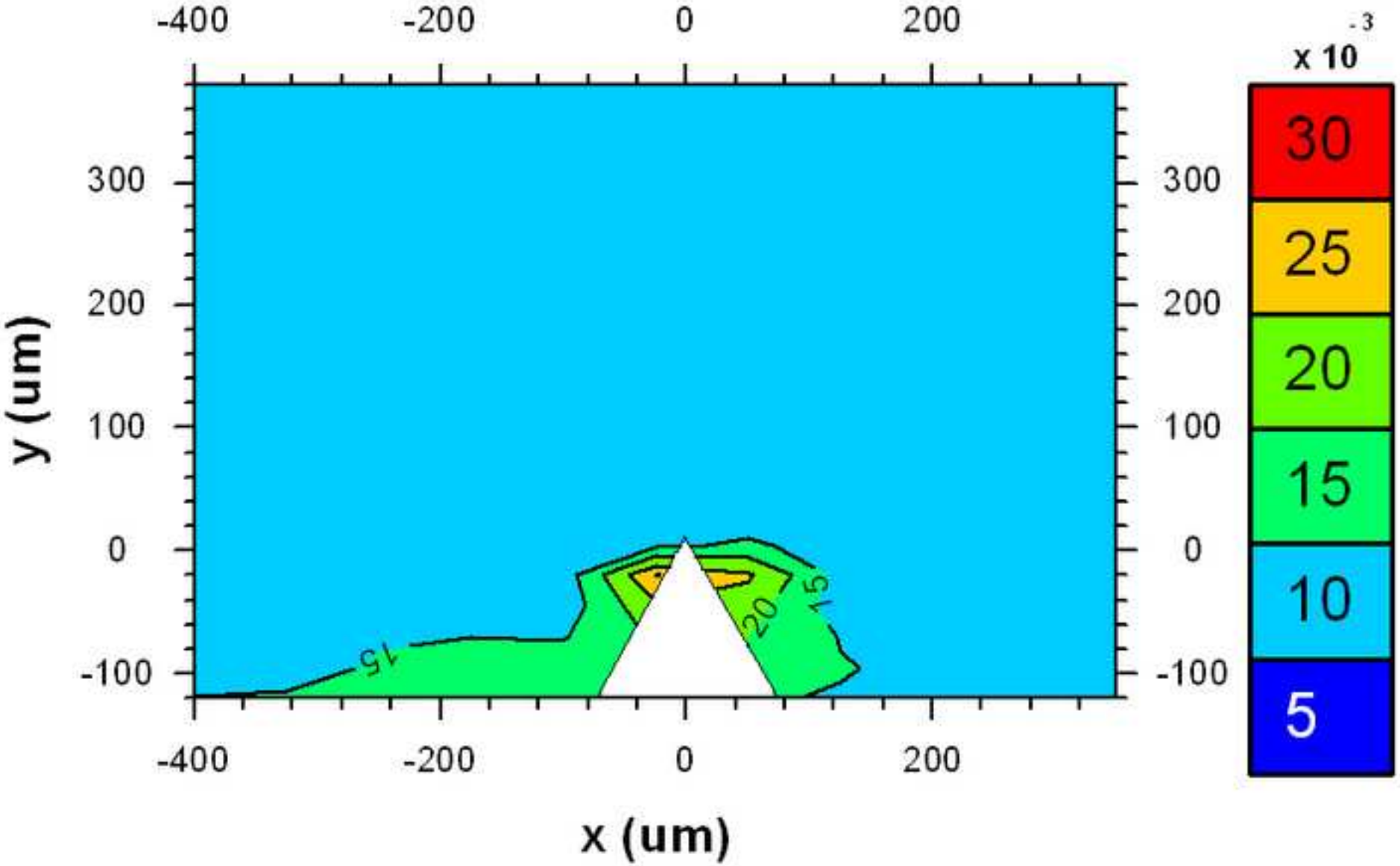
-400
-200
0
200
300
200
100
0
-100
y (um)
x (um)
x 10 -3
30
25
20
15
10
5
15
20
15

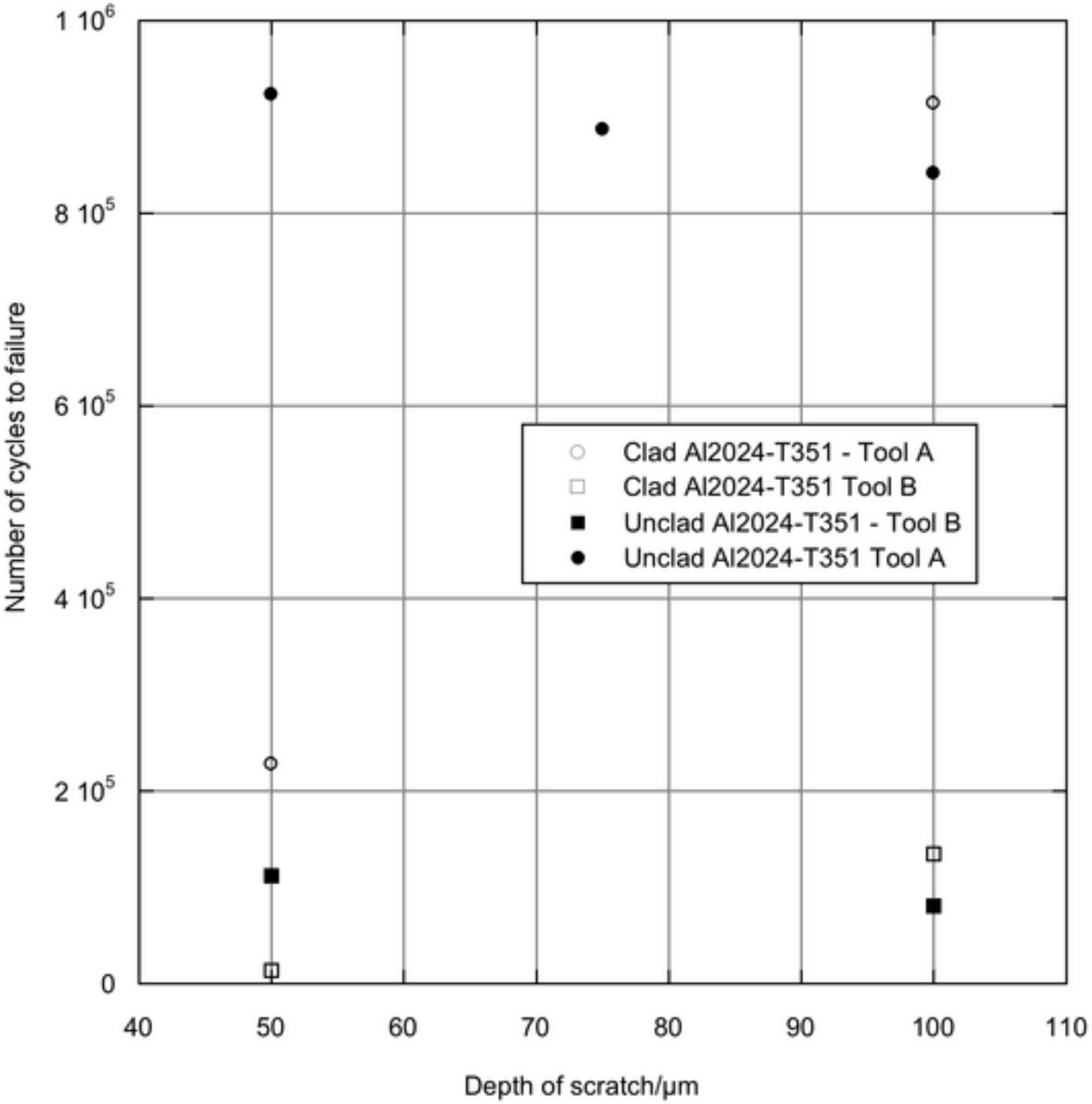

Figure 14a

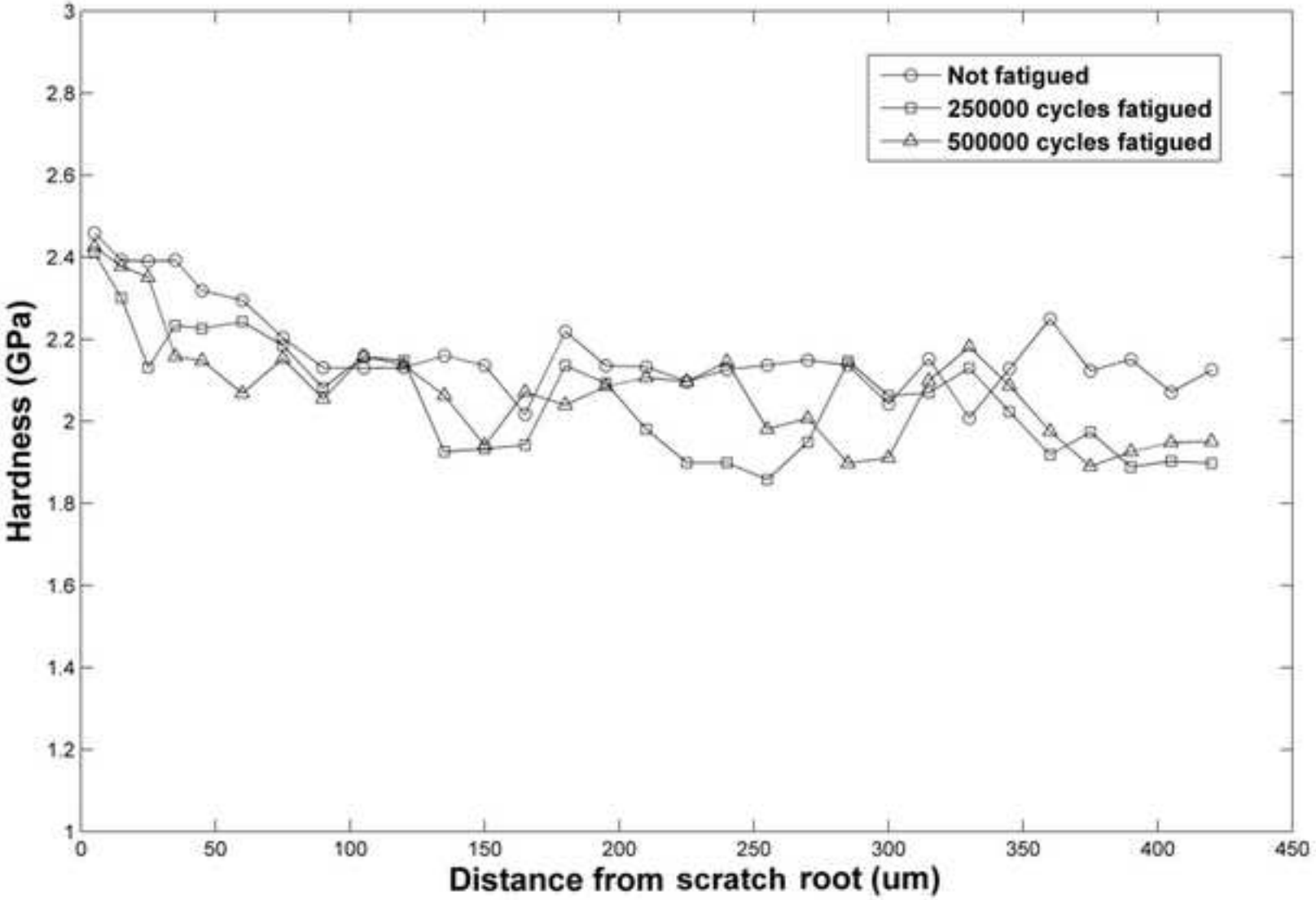
Not fatigued
250000 cycles fatigued
500000 cycles fatigued
Hardness (GPa)
Distance from scratch root (um)
3
2.8
2.6
2.4
2.2
2
1.8
1.6
1.4
1.2
1
0
50
100
150
200
250
300
350
400
450

Figure 14b

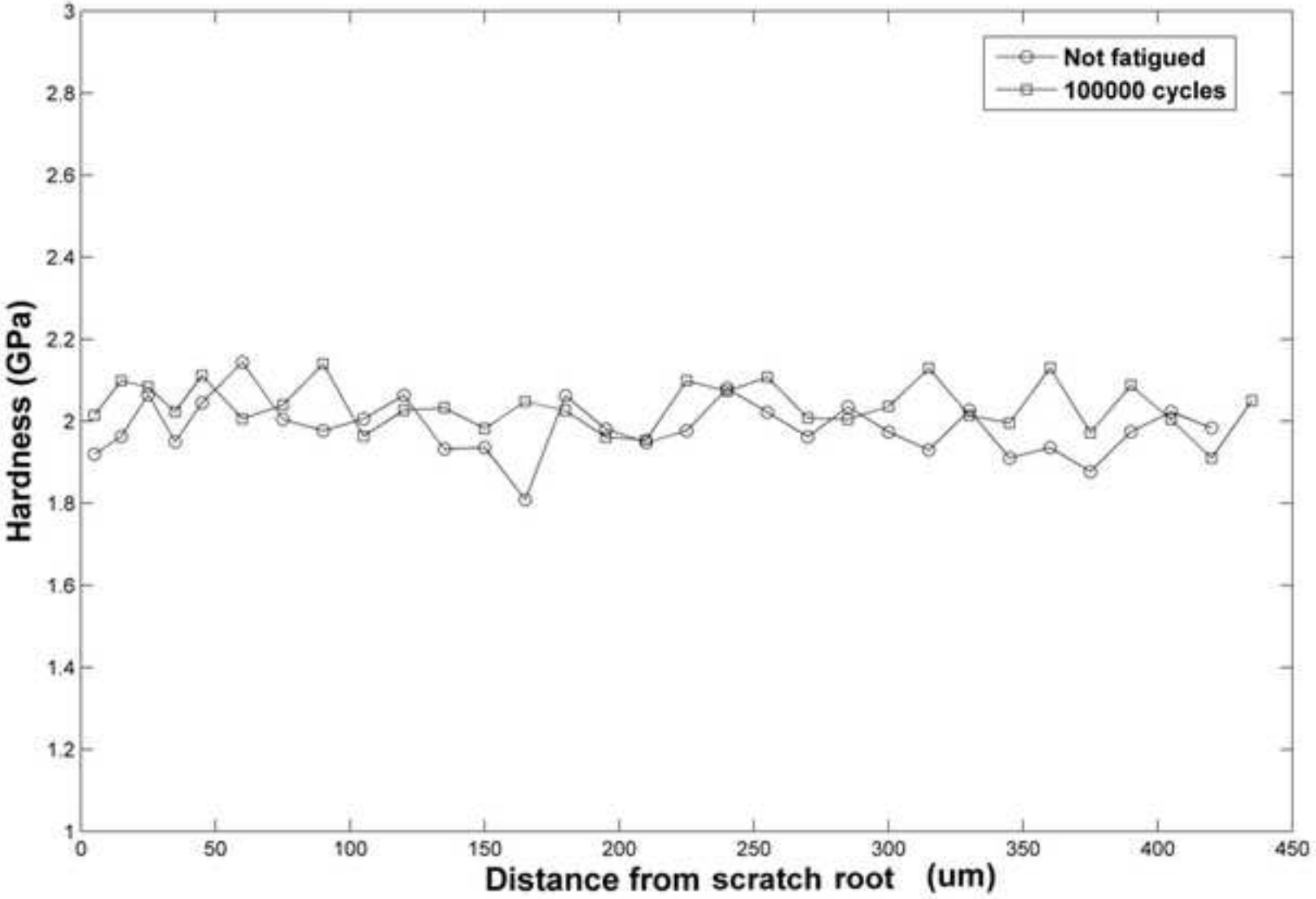
Not fatigued
100000 cycles
Hardness (GPa)
Distance from scratch root (um)
3
2.8
2.6
2.4
2.2
2
1.8
1.6
1.4
1.2
1
0
50
100
150
200
250
300
350
400
450